Computational simulation of ice accretion and shedding trajectory of a rotorcraft in forward flight with strong rotor wakes

Bidesh Sengupta[a], L. Prince Raj[b], M.Y. Cho[a], Chankyu Son[c], Taekeun Yoon[d], Kwanjung Yee[d], R.S. Myong[a,*]

[a]School of Mechanical and Aerospace Engineering and ACTRC, Gyeongsang National University, Jinju, South Korea

[b]Department of Aerospace Engineering and Applied Mechanics, Indian Institute of Engineering Science and Technology, Shibpur, Howrah, India

[c]Department of Unmanned Aircraft Systems, Cheongju University, Cheongju, South Korea

[d]Department of Aerospace Engineering and Institute of Advanced Aerospace Technology, Seoul National University, Seoul, South Korea

[*]Corresponding author: E-mail address *myong@gnu.ac.kr* (R.S. Myong)

Abstract

To ensure safe flight in icing conditions it is essential to understand ice accretion, its effect on aerodynamic performance and ice shedding in any aircraft certification program. Ice fragments shed from a rotorcraft windshield and other locations can be detrimental if they are ingested into the engine intake or impinge on the tail rotor. Because of the lack of experimental data about the forces and moments acting on ice in such a complex flow field, the computational simulation of ice shedding trajectories becomes essential. This study presents a methodology to predict the location of ice accretion and break-off, ice shape and shedding trajectory in a rotorcraft flow field with strong rotor wakes during forward flight. The methodology includes the creation of an aerodynamic database for different ice shapes (rectangle, disc, ellipse, and glaze ice shape) at various combinations of Euler angles; the analysis of rotorcraft flow field by computational fluid dynamics for different advance ratios; and a six degree-of-freedom trajectory analysis using artificial neural networks and the Monte Carlo method. The actuator surface method was applied to account for the rotor wake effect, which is capable of modeling the tip vortices and inboard sheets emanating from the rotor blades. The main results are a probability map of the ice shedding trajectory footprints on the engine intake and tail rotor planes. Disc-shaped ice fragments with a sharp edge turned out to be most dangerous. The rotation of the main rotors also substantially affected ice accretion and shed trajectory, indicating the importance of integrated simulations of all components when designing ice protection systems for rotorcraft.

Keywords: Rotorcraft; forward flight; rotor wake; ice accretion and shedding; 6-DoF; artificial neural network

1. Introduction

The accumulation of ice on aircraft flying through icing clouds is a serious risk to aircraft safety [1-3]. Alongside other safety-related accreditations before operation, icing certification is required to guarantee safe flight in icing conditions. Exposure to icing clouds for an extended period may cause significant ice accretion on critical components including wings, rotor blades, air data systems (ADS), windshield, engine inlet, fan, and propeller [4]. This accumulated ice can not only degrade aerodynamic performance but also cause ice shedding, which is a serious safety concern. A number of studies have shown that ice shedding can cause potential damage [5-8] to the sensitive components of an aircraft, which is a significant concern to the manufacturer. In general, larger ice fragments [9] have a higher potential of causing a considerable amount of damage.

In-flight icing certification of aircraft is achieved using engineering methods such as analysis [10-12] and computational fluid dynamics (CFD) [13,14], wind tunnel testing (dry and icing wind tunnels) [15-19] and flight testing (artificial ice shapes, icing tanker, and natural icing) [20-22]. The ice shedding problem can be investigated using wind tunnel tests [23] or computational simulations [24,25]. Papadakis *et al*. [23] conducted ice shedding experiments with simulated ice shapes to generate data to validate ice shedding analysis tools. They performed experiments in a dry wind tunnel to investigate the trajectories of simulated ice fragments released in the airstream during shedding. However, experimental studies using realistic ice shapes in complicated flow fields around aircraft are very rare, if not entirely absent. Furthermore, icing wind tunnel testing suffers from the very complicated scaling laws, and therefore it cannot handle all the meteorological icing conditions prescribed by an icing certification envelope.

For these reasons, the computational methods are increasingly being used to study ice accretion and shedding. It is also the only method capable of exploring the full icing envelope. Computational simulations also have the versatility to analyze any scenario or condition at low cost and, as a result, they have become the mainstream method to study ice accretion and the trajectories of ice fragments shed from aircraft.

Since the early 1980s, two-dimensional ice accretion solvers have been developed by NASA, ONEARA, DLR, and CIRA for aircraft icing research [26]. Beaugendre *et al*. [27] developed the FENSAP-ICE computational package based on the partial differential equation (PDE) which combines different modules such as impingement, ice accretion, and heat loads on a single platform. Recently, Raj *et al*. [28] investigated ice accretion and aerodynamic effects on a multi-element airfoil under the Appendix O icing envelope of supercooled large droplet (SLD) introduced in 2014. Using high-fidelity CFD and metamodeling methods, Raj *et al*. [29] systematically studied the sensitivity of ice accretion and aerodynamic performance degradation to five critical physical and modeling parameters: surface roughness, ice density, multi-shot ice model, droplet distribution, and evaporation model. Lee *et al*. [30] investigated the aerodynamic characteristics and complex interactions between flows generated from iced airfoils with three multi-elements—slat, main, and flap—using large-eddy simulations.

Cao *et al*. [31] summarized the computational models available for helicopter icing, including aerodynamics, ice accretion, the performance of icing protection system (IPS), and the effects of icing on helicopter performance. Szilder [32] calculated the impingement of droplets on the fuselage and rotors of a Bell 412 helicopter in forward flight using the Lagrangian approach. Aliaga *et al*. [33] computed ice shapes by updating the geometry of the iced surface in time and simulated the rotating/stationary interactions using dynamically stitched grids. Ahn *et al*. [34] conducted an experimental study on the engine air intake of a KUH-1 Surion helicopter using an icing wind tunnel to obtain the shape of ice accretion and compared the experimental results with the FENSAP-ICE computational package. Jung *et al*. [35] evaluated the performance of electrothermal anti-icing systems for a rotorcraft engine air intake based on a meta model and presented guidelines for determining the required level of heater power and the size of heat pads.

Ice shedding or ingestion beyond a threshold (for example, 130 grams in the case of the engine intake) into the critical component of an aircraft can be very dangerous. For instance, in an accident on 2nd January 2013, Eurocopter EC130B4 experienced a hard landing due to engine power loss, and as a consequence the pilot and three medical crew were seriously injured. The report by the National Transportation Safety Board (NTSB) concluded that the engine power loss

occurred due to significant deformation of the outboard tips of four compressor blades in the engine in the direction opposite to normal rotation, due to the impact of foreign object debris such as ice [36]. In another accident on 17th January 2012, Eurocopter AS350B3 C-FMPG was destroyed in British Columbia and the pilot was killed. According to the Aviation Investigation Report A12P0008 [37], the engine power loss and hard landing occurred because of damage of the compressor blade from ice ingestion.

Therefore, ice shedding, an aftermath event of ice accretion, can be of serious concern to the safety of the aircraft as shown by various accident reports. To tackle this problem, various researchers in the past have attempted to predict ice accretion and ice shedding and its trajectories and to prevent collisions of ice fragments with critical parts of the aircraft. Ignatowicz *et al*. [38] established a link between the static moment and dynamic moment acting on an ice fragment in a one-way coupled computational simulation. Anthony *et al*. [39] and Hayashi *et al*. [40] developed computational models by combining ice accretion and ice shedding and predicted the occurrence times of ice shedding and the mass of shed ice. Papadakis *et al*. [9,23] proposed a method to utilize six degrees-of-freedom (6-DoF) and Monte Carlo simulations to compute ice trajectories and probability footprint density for a business jet aircraft. Dong *et al*. [41] presented inflight parameter identification and icing location detection of an aircraft and generated an icing detection block, based on a probabilistic neural network. Sathyanarayana *et al*. [42] examined the accuracy of the two-way coupling method with dynamic meshing in an ice trajectory calculation.

The flow field generated by a rotorcraft is extremely complicated due to interactions between the rotor blades and fuselage. The resulting flow structures are characterized by highly spatially non-uniform, highly three-dimensional, and unsteady fields. The vortices and the wakes produced by the rotor blades and their interactions are also highly dependent on the advance ratio [43-46]. A general flow field [47-51] around a rotorcraft with four blades is depicted schematically in Fig. 1. The essential features in the flow-field of rotorcraft in forward flight are the inflow and the downwash. A large amount of air is taken through the rotor and pushed downwards. The advance ratio of the rotorcraft determines the direction of the downwash and the interaction of downwash with the tail region of the helicopter.

In forward flight, the component of freestream velocity adds or subtracts from the rotational velocity of the blade depending on the direction of the blade, i.e., whether the blade is approaching or moving away from the freestream. Although the velocity distribution along the blade remains linear, it is no longer axisymmetric and varies with respect to azimuthal angle. In addition, the forward flight speed, blade pitch angle, and distribution of induced inflow through the rotor disk will affect the angle of attack on the blade, and therefore lift distribution, rotor thrust, and power consumption. Moreover, high dynamic pressure at the tip of the rotorcraft blade produces a high concentration of aerodynamic force, resulting in strong vortices near each blade tip. These are a series of interlocking vortices with almost helical trajectories, also known as tip vortices, as shown in Fig. 1. These tip vortices remain close to the rotor, following the rotor for several revolutions. The interaction between these vortices and the following blades produces a strong three-dimensional induced velocity field. The interaction between the following blades and induced velocity field, fluctuating air loads, results in the fluttering of blades producing local vortices of various scales. The interaction between these vortices and fuselage also produces several flow structures with a high level of spatial inhomogeneity.

The characteristics of ice accretion on a rotorcraft surface are directly affected by the aerodynamic interaction between the strong vortices and the fuselage. The mechanism of ice break-up from the surface is intricate and inherently stochastic. The mechanical properties of ice are dependent on the ambient temperature, rate of freezing, presence of porosity, and micro-impurities. A change in microstructure can change the macroscopic properties of ice, such as its strength. Moreover, the rapidly changing flow field around the ice promotes ice break-up, making the whole process stochastic. The interactions between vortices, fuselage, and variation in the overall flow field due to forward flight speed creates an intricate flow field. For instance, Son *et al*. [52] investigated the complicated flow field of a rotorcraft due to rotor-wake effects and subsequent ice accretion on rotorcraft fuselage.

However, very few studies have addressed ice shedding in a flow field of a realistic rotorcraft with multiple blades. Previous studies in this field were restricted to the analysis of simple configurations like airfoils and the flow fields of fixed-wing aircraft with simplified ice shapes.

There are few studies on ice shedding trajectory and footprints in the flow field of a rotorcraft with multiple blades with realistic ice shapes. To address this shortcoming, this study develops a general methodology to predict the location of ice accretion, ice shape and shedding trajectory in a rotorcraft flow field with strong rotor-wakes in forward flight. It focuses on critical factors such as flow conditions, ice shapes, and break-off orientations that influence the ice footprints. This level of detailed study will be essential to fully understand the effects of the critical factors on the footprints of ice shedding trajectory, and for the design of proper ice protection systems (IPS) for rotorcraft in the future.

The present methodology includes the identification of the location of ice accretion and break-off; the creation of an extensive aerodynamic database for different ice shapes (rectangle, disc, ellipse, and glaze ice shapes) at various combinations of Euler angles; the computation of complicated rotorcraft flow fields using computational fluid dynamics (CFD); and a 6-DoF trajectory analysis using artificial neural networks and the Monte Carlo method. To take into account for the rotor wake effect, the actuator surface method (ASM) was applied, which is capable of modeling the tip vortices and inboard sheets emanating from the rotor blades. A key component of the present methodology is an integrated computational simulation of ice accretion and shedding trajectory of rotorcraft in forward flight taking into account the interaction of the fuselage and rotor blades. The final results are the probability map of the footprints of ice shedding trajectories on the engine and tail rotor plane.

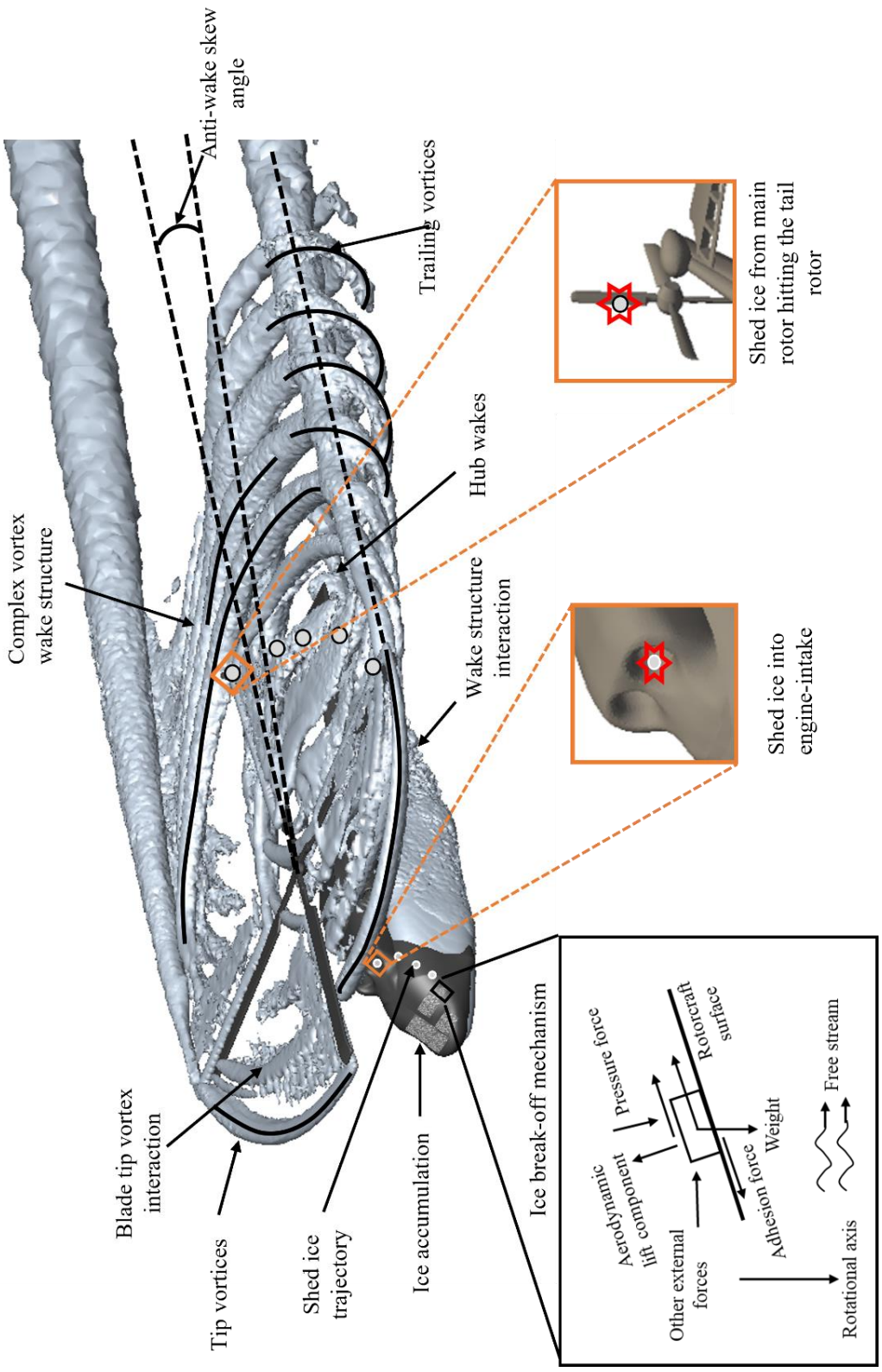

Fig. 1. A schematic diagram of the flow field of a rotorcraft with four blades and ice break-off mechanism.

2. Mathematical modeling of rotorcraft flow field and ice shedding

This section describes the rotorcraft flow field and the mechanisms of ice break-off from the surface, together with probable representative ice fragments. The simulation of ice trajectories was achieved by combining a 6-DoF code, artificial neural network (ANN) and Monte Carlo methods.

2.1. Numerical methodology for the computation of rotorcraft flow field and ice accretion

For the data related to the flow fields of the rotorcraft and ice accretion shapes with various forward flight speeds, we used a method developed in previous studies [28,52]. The simulation method is composed of four different modules: 1) a flow analysis module based on the Navier-Stokes-Fourier (NSF) equations and the ASM, 2) a droplet-trajectory analysis module based on the Eulerian droplet equation of shallow water type [53,54], 3) a PDE-based thermodynamic module, and 4) a grid-regeneration module. We employed two approaches when predicting ice accretion: 1) single-shot, where the ice accretion is calculated entirely based on initial flow field data, and 2) multi-shot, where the air and droplet flow field data are updated based on changes in the ice accretion for a specified number of times, as shown in Fig. 2.

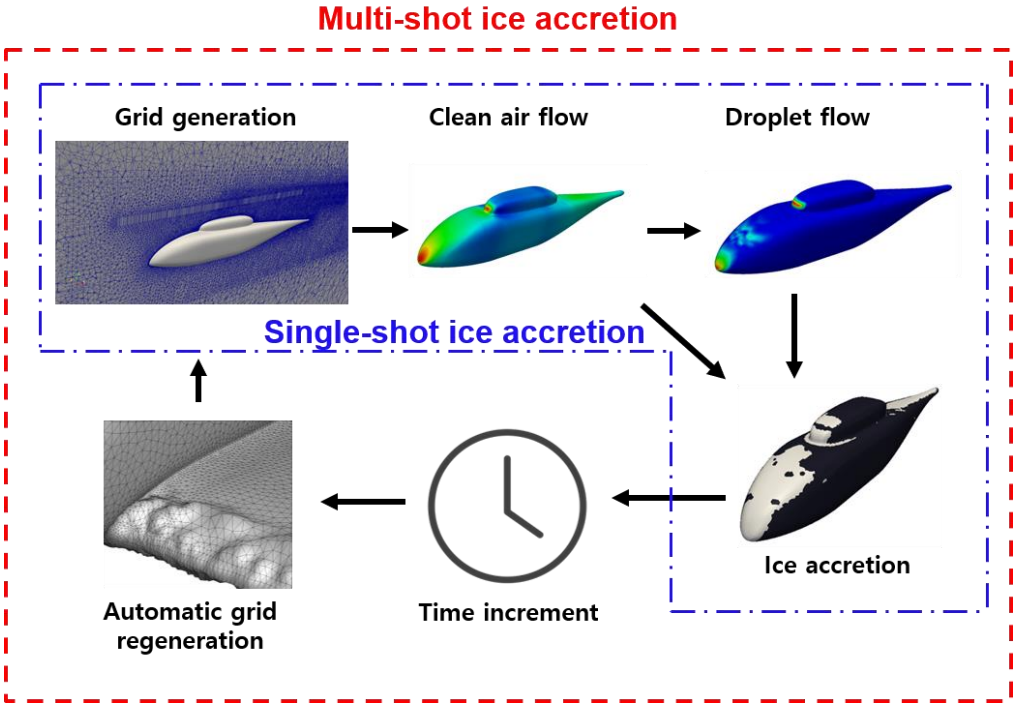

Fig. 2. Methodology for single-shot and multi-shot ice accretion processes.

The droplet-trajectory analysis module is based on the shallow water type Eulerian droplet equation with source terms, as summarized in appendix A. The mass of impinging droplets can be computed from the velocity and bulk density of the droplet field. The thermodynamic analysis module then determines the fraction of the mass that freezes on the surface, as described in appendix B. The thin water film theory is used to describe the behavior of unfrozen water on the surface. The phase change from the impinged water to freezing ice is calculated based on the Messinger model. Finally, the ice thickness is determined using the value of ice density in the grid-regeneration module. Further details about the present method of ice accretion and its validation can be found in [28,52].

The icing exposure time is substantially longer than one revolution of rotation. Thus, performing a full unsteady simulation through the four modules is impractical. In the present simulation, after ten rotor revolutions, the velocity vector fields were averaged using the last rotor revolution, which was later used for the droplet-trajectory calculation.

Since this study focuses on icing on the fuselage and the trajectories of the ice fragments detached from the fuselage surface, it is necessary to consider the strong wake induced by the main rotor. To efficiently account for the rotor wake effect, we incorporated the ASM into the NSF flow analysis module. The ASM is capable of modeling the individual tip vortices and inboard sheets emanating from the rotor blades.

The ASM was originally developed for wind turbine applications under the incompressible condition without energy conservation [55]. However, heat transfer between the air and the surface is important for icing simulations. To this end, in the present study the incompressible ASM was extended to the compressible NSF equations. The ASM incorporates the effect of an individual rotor blade as the source term in the momentum equation, as follows,

$$\frac{\partial(\rho\vec{u})}{\partial t}+\nabla\cdot\left(\rho\vec{u}\vec{u}\right)=-\nabla p+\nabla\cdot\left(2\mu[\nabla\vec{u}]^{(2)}\right)+\frac{d\vec{T}}{dV} \tag{1}$$

where μ, $d\vec{T}$, dV represent the viscosity of air, the local thrust and the volume of the cell, respectively. The added source term in (1) is determined from the calculated thrust for the

computed volume of the rotor blade, and it becomes zero for other computed volumes. In this way, the source term imposes a pressure jump in the computation cells representing the exact location of the rotor blades. Similarly, the energy conservation for the present compressible ASM was modified as

$$\frac{\partial(\rho h)}{\partial t}+\nabla\cdot\left(\rho h\vec{u}\right)+\frac{d\left(\rho K\right)}{dt}+\nabla\cdot\left(\rho\vec{u}K\right)-\frac{\partial p}{\partial t}=\nabla\cdot\left(\alpha\nabla h\right) \tag{2}$$

where h denotes the enthalpy per unit mass, $K\equiv|u|^2/2$ represents the kinetic energy per unit mass, and h denotes the thermal diffusivity of air.

2.2. Identification of ice break-up, shape, and location

Ice break-off from the surface is mainly the result of two processes: 1) loosening of the bond between the ice and the surface of the structure, and 2) crack development and propagation inside the ice. The breaking of the bond between the ice and surface may be caused by the action of deicing equipment, or very high centrifugal force, or the application of an external force such as wiper movement, or the combination of two or more of the aforementioned factors. In addition, varying flow fields around the rotorcraft and structural vibration may produce substantial fluctuating forces on the ice, leading to the accumulation of fatigue inside the ice. Subsequently, the fragment breaks from itself because bonding force inside the ice has weakened.

Ice accreted on the surface is subjected to various kinds of forces. The free body diagram of the forces that can act on the ice is shown in Fig. 3. As the ice is subjected to the flow field, three aerodynamic forces (drag, lift, and side force) will act on the ice. Moreover, if the ice is subjected to rotational motion, as in the case of a helicopter rotor or turbofan, the ice will experience a large centrifugal force [56]. In addition to these forces, other external forces can exist, such as those imposed by wiper movement, or deicing equipment like electro-mechanical expulsive systems. On the other hand, the aerodynamic pressure force and the weight of the ice act against the break-up of ice. Most importantly, as the ice accretes on the surface, a strong adhesion force forms at the interface between the ice and the surface (steel, or aluminum, or composite) [57,58].

For ice which has accreted on the fuselage of the helicopter, where centrifugal force is absent,

the combined effect of aerodynamic forces and other external forces or their interactions will determine the break-up of ice from the surface. The formation and break-up of ice are inherently local phenomena, since droplet impingement and aerodynamic forces on the fuselage vary in different locations, and deicing by the wiper on the windshield is position-dependent.

Ice exhibits a variety of physical behaviors ranging from ductile to brittle as a function of strain rate and temperature [59-61]. The mechanical properties of ice show a strong dependence on temperature, rate of freezing, porosity, and micro-impurities [62]. Ice may experience dynamic fluctuating forces due to the dynamic flow field and structural vibration. After sufficient cycles of these fluctuating loads, fatigue appears inside the ice and the strength of the ice decreases, leading to very early failure. The amplitude of the fluctuating load determines the number of cycles the ice can sustain before breaking off [56,63].

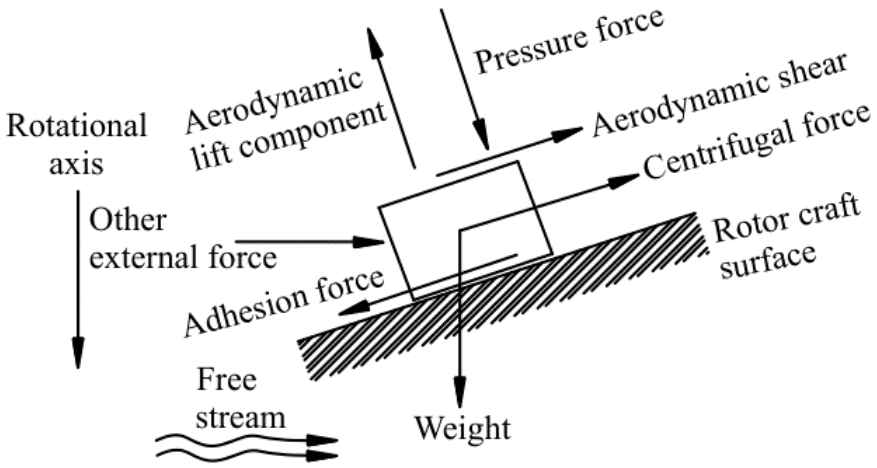

Fig. 3. Different possible forces that can act on ice fragment subjected to various flow field conditions.

Other external forces usually initiate the ice break-up process, and the aerodynamic forces then contribute to the process and enhance it. The deicing system periodically removes ice by mechanical or thermal means and plays an initial role in the ice break-up process [64]. In the case of the windshield, the movement of wipers plays a significant role in initiating ice break-up. The

movement of the wiper will carry the ice with it until the wiper reaches the curved surface of the windshield, where the ice will have a high tendency to tear off from the surface and move along with the strong airflows. The movement of the wiper may also cause a temporary accumulation of ice at the upper tip of the wiper during operation. When that accumulation becomes large enough that the adhesion force between the ice and the surface is smaller than either the weight of the ice chunk or the aerodynamic force due to its large size, the ice chunk will break off from the surface.

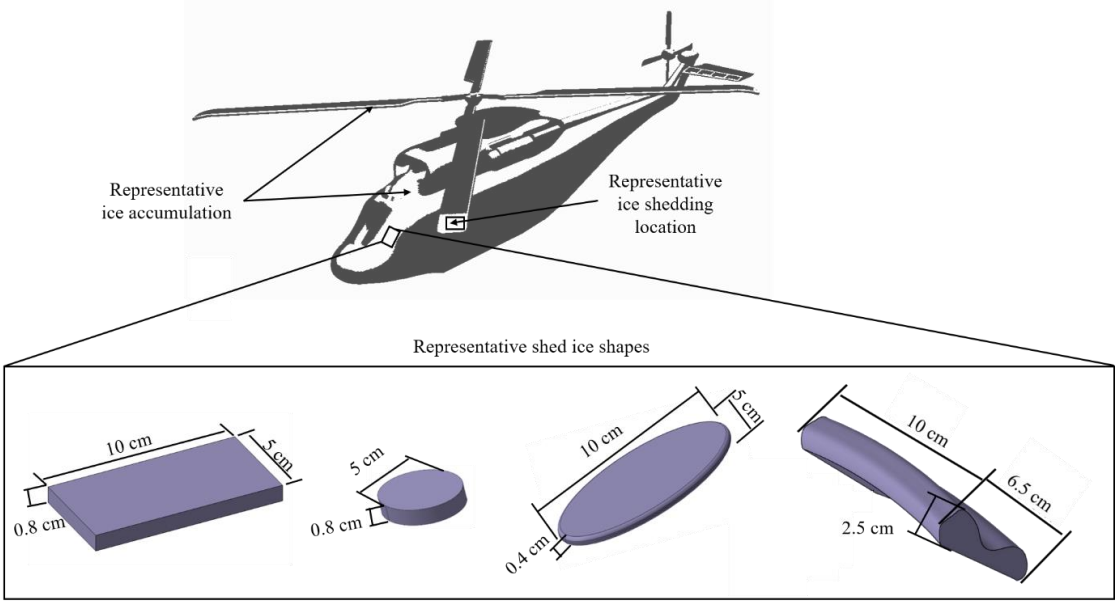

Fig. 4. Representative shapes of ice break-off from the surface: (a) rectangle, (b) disc, (c) ellipse, and (d) glaze ice shape (GIS).

Considering those scenarios of ice break-off during the forward flight of a helicopter, there can be at least four probable representative shapes of ice shed from the surface of a helicopter fuselage including the windshield, as depicted in Fig. 4.

Rectangle or plate: When the ice accretes over a flat surface of the fuselage or the windshield, the ice has a large surface area and small thickness. When any breaking force is large enough to tear the ice from a flat and smooth surface, the broken ice piece will have a shape that resembles a rectangle or plate.

Disc: During the movement of the wiper, some ice may accumulate at the tip of the wiper. The movement of the wiper can create a torque on the side of the accumulated ice, giving the ice the

approximate shape of a disc.

Ellipse: When the ice accretes over a flat surface of the fuselage or the ice accumulates over the wiper during its movement, and the ice size becomes enough that the aerodynamic force on it becomes large, the chunk may break off and take the shape of a rounded edge bar, much like the shape of an ellipse.

Glaze ice shape (GIS): GIS forms when ice accumulates from the accretion and refreezing of the run-back water after melting. The run-back water moves in the downstream direction due to the aerodynamic drag of the wind and refreezes after losing its latent heat, forming irregular shapes. GIS can form at the boundary of the anti-icing region of a windshield embedded with electrothermal heating thin film, or near the leading edge of a rotor blade moving with high speed. Because of its sensitive location near the engine intake and the potential path of the initial break-off, the trajectory of shedding GIS should be treated very carefully.

The ice shedding (or break-off) location is primarily determined by where the ice has substantially accreted under given icing and flight conditions. The shedding location and shape of the ice that might impact a critical component of the rotorcraft are of the utmost importance. As discussed earlier, however, the formation and break-off of ice are local phenomena and dependent on many factors. In particular, the break-off of ice is inherently stochastic.

Because of the random nature of ice shedding, it is very difficult to predict the exact location ice shedding. For this reason, stochastic methodology was adopted to determine the location of ice shedding. We first selected several shedding locations and then performed a hundred 6-DoF simulations with different sets of Euler angles for each of these locations to find the shedding locations with high probability. It turned out that in most locations, no or very few ice fragments reached the engine plane of the rotorcraft, while ice fragments from some locations could reach the engine plane. The locations from where at least fifty percent of ice fragments reach the engine plane were considered. The collection of these locations that were very close to each other were then represented as one shedding location. The most crucial shedding locations are designated ‘A’,

'B', 'C', 'D', and 'E' in Fig. 5.

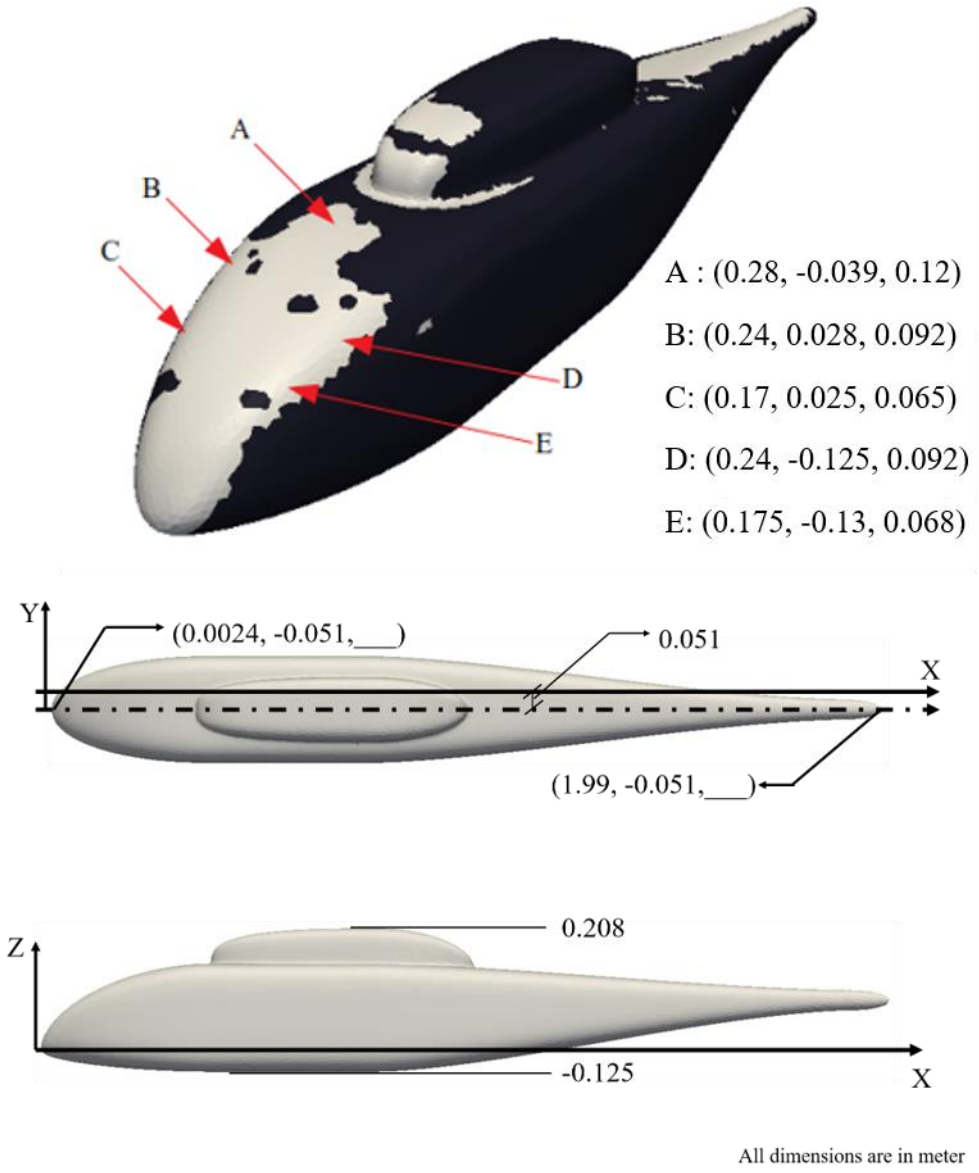

Fig. 5. Representative locations (with coordinates) where ice break-up and shedding are near critical components of the rotorcraft.

2.3. Six degrees-of-freedom simulation method

Ice fragments subjected to an airstream experience three forces (normal, axial, and side force) and three moments (pitching, yawing, and rolling moment). The 6-DoF method describes the translational motion resulting from the forces, and the rotational motion due to the moments, that act on the fragment. The spatial acceleration of the body in the inertial frame can be derived from the vector summation of three-body forces, and then transforming them into the inertial frame.

The spatial acceleration in the body frame can be calculated from the following equations [65,66],

$$\begin{aligned} \ddot{X}^x &= \frac{1}{m} F_x^b + g^x, \\ \ddot{X}^y &= \frac{1}{m} F_y^b + g^y, \\ \ddot{X}^z &= \frac{1}{m} F_z^b + g^z. \end{aligned} \tag{3}$$

Here F_x^b, F_y^b, F_z^b represent the axial, side, and normal forces being exerted on the ice fragment, respectively. The superscript *b* represents the body (non-inertial) reference frame. $\ddot{X}^i, m, g^i$ represent the acceleration and mass of the body (ice fragment) and gravity, respectively. The velocity and displacement of the body can be calculated by subsequent integration of the equations.

The rotational motion of the body governed by the Euler's equation of motion can be expressed as

$$\vec{M}^b = \frac{d\vec{H}^b}{dt} + \vec{\omega}^b \times \vec{H}^b. \tag{4}$$

Here $\vec{M}^b, \vec{H}^b, \vec{\omega}^b$ represents the moment, moment of momentum, and angular velocity acting on the body, respectively, with respect to the body frame. The angular acceleration can be determined as (*I* denoting the inertia matrix)

$$\frac{d\vec{\omega}^b}{dt} = I^{-1}\left[\vec{M}^b - \left(\vec{\omega}^b \times \vec{H}^b\right)\right]. \tag{5}$$

Considering the angular velocities P, Q, R about the body axes x_x^b, x_y^b, x_z^b, respectively, this equation can be further expanded in terms of the moments acting on the body axes,

$$\begin{bmatrix} \dot{P} \\ \dot{Q} \\ \dot{R} \end{bmatrix} = \begin{bmatrix} I_{xx} & I_{xy} & I_{xz} \\ I_{yx} & I_{yy} & I_{yz} \\ I_{zx} & I_{zy} & I_{zz} \end{bmatrix}^{-1} \left(\begin{bmatrix} M_x^b \\ M_y^b \\ M_z^b \end{bmatrix} - \begin{bmatrix} P \\ Q \\ R \end{bmatrix} \times \begin{bmatrix} I_{xx} & I_{xy} & I_{xz} \\ I_{yx} & I_{yy} & I_{yz} \\ I_{zx} & I_{zy} & I_{zz} \end{bmatrix} \begin{bmatrix} P \\ Q \\ R \end{bmatrix} \right). \tag{6}$$

where M_x^b, M_y^b, M_z^b represent rolling, pitching, and yawing moments.

The angular velocities can be obtained by integrating the angular acceleration from Eq. (6) in the body frame. The quaternion ($q = [q_1, q_2, q_3, q_4]$) rates can then be calculated from the angular velocities as follows [65],

$$\begin{aligned}
\dot{q}_1 &= -\frac{1}{2}\left(q_2 P + q_3 Q + q_4 R\right) + \lambda q_1, \\
\dot{q}_2 &= \frac{1}{2}\left(q_1 P + q_3 R - q_4 Q\right) + \lambda q_2, \\
\dot{q}_3 &= \frac{1}{2}\left(q_1 Q + q_4 P - q_2 R\right) + \lambda q_3, \\
\dot{q}_4 &= -\frac{1}{2}\left(q_1 R + q_2 Q - q_4 P\right) + \lambda q_4.
\end{aligned} \tag{7}$$

Here the drift correction gain λ is given as $\lambda = 1 - (q_1^2 + q_2^2 + q_3^2 + q_4^2)$. The quaternion rates can be numerically integrated to obtain new sets of quaternions at the next time step. The Euler angles (ψ, θ, ϕ) can be obtained from the sets of a new quaternion using the following equations

$$\begin{aligned}
\psi &= \cos^{-1}\left(\frac{q_1^2 + q_2^2 + q_3^2 + q_4^2}{\cos\theta}\right)\left(\text{sign}\left[2\left(q_2 q_3 + q_1 q_4\right)\right]\right), \\
\theta &= \sin^{-1}\left[-2\left(q_2 q_4 - q_1 q_3\right)\right], \\
\phi &= \cos^{-1}\left(\frac{q_1^2 - q_2^2 - q_3^2 + q_4^2}{\cos\theta}\right)\left(\text{sign}\left[2\left(q_2 q_4 + q_1 q_2\right)\right]\right).
\end{aligned} \tag{8}$$

2.4. Generation of footprints using artificial neural network

An artificial neural network (ANN) follows the strategy of adaptation, by which it learns and evolves. A neural network is a deep learning method in which multiple neurons are used in each layer, called hidden layers, in between the input and output layers. Each neuron is connected with every neuron in the former and later layers by a certain number of variable weights. Sometimes some bias can be added to a neuron. The output from the neuron becomes the linear summation of the multiplication of weights and values of the connected neurons [67]. This value is multiplied

with a non-linear function called an activation function to bring non-linearity to the calculation. Therefore, the output of each neuron can be written as [68],

$$u = \sum w_i x_i + b_i. \tag{9}$$

Here w_i represents the weights of the connections with b_i as bias on the neuron. The resultant function u is formed as a function of the inputs (x_i), weights (w_i), and bias (b_i). After multiplication of the activation function such as sigmoid and ReLu (Rectified Linear Unit), a quantity can be expressed as the multiplication of the activation function with the neuron output,

$$y_k = f(u). \tag{10}$$

The training data from the test cases are provided to the input layer, from which it propagates to the output layer, and weights are assigned to the connections, a process known as forward propagation. The initial output values vary from that of the original output that was provided in the test case. Thus, the accuracy of the system is measured by cost function or loss function, which is defined as

$$C = \frac{1}{N} \sum_k \left(y_k - a \right)^2, \tag{11}$$

where *N* denotes the number of training inputs, *a* is the predicted value, and *y* is the actual value. The aim here is to minimize the value of cost or loss.

In the present study, a gradient descent optimization algorithm was used to minimize the cost. During the forward propagation, random weights and biases were assigned to the connections. The calculated error from the forward propagation was then fed back along with the gradient of the cost function to update the weights to reduce errors in the subsequent iterations, a process known as backpropagation. The whole process was repeated until a high enough accuracy was achieved.

The training data in the present study were generated by the 6-DoF code to train the network.

After training the network with different sets of hidden layers, and the number of neurons required to achieve an accuracy of at least 99%, the network was used for further computational simulations.

2.5. Monte Carlo simulation

The break-off of ice from the surface is inherently stochastic and depends on a large number of parameters. Important factors include the break-off location, orientation, shape, size, weight, variation of density inside the ice, aerodynamic characteristics, and underlying rotorcraft flow fields that carry fragments. Therefore, a probabilistic method such as the well-known Monte Carlo [69,70] is needed to account for the random feature of ice shedding.

For the Monte Carlo simulation, firstly, one needs to identify the important factors affecting the randomness in the problem. Secondly, one needs to define a proper probability distribution for each parameter. Then for each variable, one needs to determine the value randomly within the range of possible values obtained by the cumulative probability distribution. The probability distribution was obtained by creating a grid system (800×800) on the ANN maps and then introducing the ratio of the number of hits in a particular cell to the total number of hits. The cumulative probability distribution was used to form an interval table. Next, a large number of random numbers were generated, and events were selected based on the matches between the generated random numbers and the intervals. The number of repeated events was then added. Finally, the outcome of the problem can be obtained by iterative computation.

In the present study, we used the Monte Carlo method to obtain the probability maps of ice fragment footprints on the engine intake and tail rotor planes, downstream of the shedding location. These maps were then utilized to determine how severely the critical components of the rotorcraft were exposed to the shedding of ice fragments. Random unbiased initial orientations were considered in the Monte Carlo simulation for five different locations on the frontal fuselage of the rotorcraft, four different ice shapes, and four different flow fields with the advance ratios of 0.075, 0.15, 0.2, and hovering.

2.6. Summary of methodology

The primary purpose of this study is to investigate the probability of ice shedding footprints on the engine intake and tail rotor planes. This was accomplished by combining the helicopter flow field including the strong rotor wake, 6-DoF computations with ANN, and Monte Carlo simulation. The flow chart of the general methodology is described in Fig. 6. In the beginning, the airflow and droplet fields of the rotorcraft were generated for given flight and icing conditions. As the ice accretes with time, the airflow field around the rotorcraft changes continuously. However, this transient behavior was not taken into consideration in the present study, as the effect of wakes is far stronger than the change in flow field produced by ice accretion. After running the PDE-based thermodynamic module for ice accretion, we identified the probable location and condition of ice break-off from the frontal part of the fuselage of the rotorcraft.

The aerodynamic database of the most probable ice shapes was generated in advance with the help of an NSF-based CFD code for a combination of Euler angles. The aerodynamic data and airflow field were then fed into the 6-DoF code. It is mathematically a one-way coupling in which the motion of ice is affected by the airflow field but not vice versa, which is well justified in the case of small moving objects like ice fragments. The initial coordinates and angular orientations of the ice fragment were selected from the probable location and condition of ice break-off. The forces and moments on the ice fragment were calculated based on the pre-generated aerodynamic database. The time marching was achieved using the fourth-order Runge-Kutta method. In this way, the shed ice fragment travels in the flow field as time advances. At the end of the simulation, the ice footprint data from the engine inlet and tail rotor planes were collected.

Next, the ANN module was utilized to predict a large number of trajectory outputs with the given set of Euler angles as input. The ANN was trained using the data generated by the 6-DoF code in advance. After the ANN was trained to a sufficiently high level (at least ninety-nine percent accuracy), it was used for further simulations. The Monte Carlo module was then employed to perform the stochastic simulation using the ANN data. The Monte Carlo simulation provides the most probable maps of trajectory footprints on critical parts of the rotorcraft for a large number of parameters.

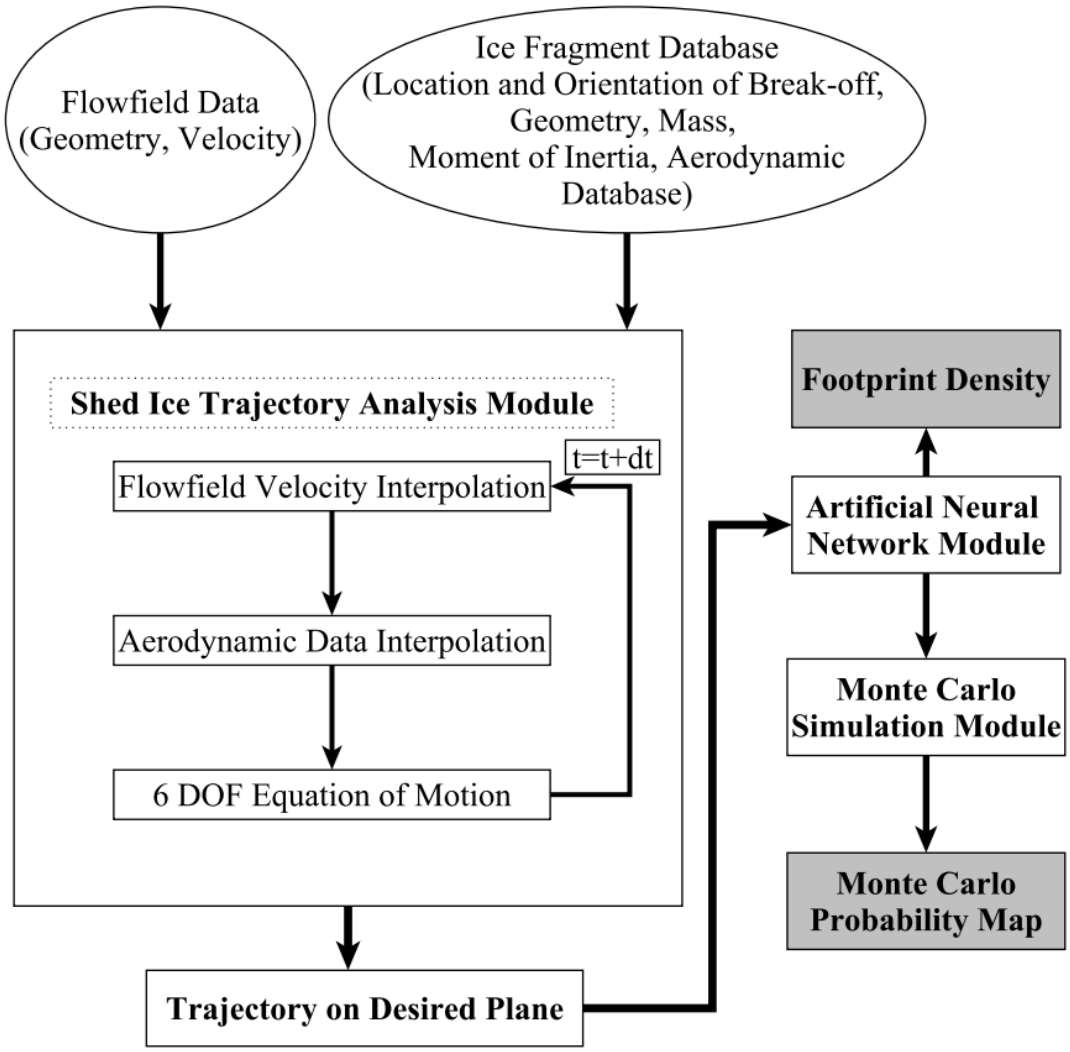

Fig. 6. Flow chart of ice shedding simulation methodology.

3. Rotorcraft flow field, ice accretion, and ice shedding trajectory

To obtain the shapes of ice accretion on the fuselage of a rotorcraft, we chose the ROBIN (ROtor Body INteraction) body [71,72] as a representative configuration. We then conducted a computational simulation for 30 minutes using the metrological icing condition defined by LWC of 0.6 g/m^3, MVD of 20 μm, and the ambient temperature of -10°C. We selected four cases with advance ratios of 0.2, 0.15, 0.075, and 0 (hovering). The forward flight of the rotorcraft will result in ice formation on the frontal surface of the fuselage. Although a long exposure time of 30 minutes

was considered, the absolute forward flight velocity of the rotorcraft (38 m/s in the case of advance ratio of 0.2) is lower than that of a conventional fixed wing aircraft. As a result, the ice accreted on the fuselage belongs to rime (or intermediate) ice according to Dickey's data [73] in determining the form of an ice accretion. Therefore, there was no significant difference in the rate of surface change even though there was a slight difference in the shape of accreted ice between the single-shot and multi-shot calculations. From these observations, the final icing shape can be obtained using the single-shot method, which can greatly reduce the computation time.

3.1. Numerical simulations using the aerodynamic and ice accretion solvers

To identify the location of ice break-off, one needs to determine in advance the region in which ice accretion occurs. However, there is no published data for local ice accretion on a rotorcraft (or helicopter) fuselage, obtained using icing tunnels or natural icing tests. Accordingly, we obtained the ice accretion shapes for three forward flight speeds and the hovering case, using computational simulations. The rotor wake structures, the ice accretion shapes, and the mass distribution of ice accreted on the fuselage for the four flight cases are illustrated in Figs. 7, 8, 9, respectively.

In the highest speed case (μ=0.2), the strong tip vortexes of the main rotors formed but did not collide with the frontal surface of the fuselage, as shown in Fig. 7 (a). As can be seen in Figs. 8 (a) and 9, most of the frontal surface of fuselage including the windshield and the engine intake section is covered with ice due to the inflow of the strong rotor wakes. The ice accreted on the frontal surface of the fuselage is thicker than in the lower speed case because of the higher rate of droplets impinging on that region during high flight speed. The tail boom region is also covered with ice, since the strong tip vortexes collide on that region.

In lower-speed cases (μ=0.15, 0.75), the ice accretion at the nose and tail boom regions was prominent, as shown in Figs. 8 (b),(c) and 9. Because of the wake skew angle, the windshield area was less affected by inflows than in the high-speed case. However, thicker ice was observed on the tail boom region, because most of the tail boom region is still located under the inflow of the rotor wakes, as shown in Fig. 7 (b), (c).

In the hovering case (μ=0), there was no ice accretion at the nose, as expected from the zero-

forward velocity, as shown in Figs. 7 (d) and 8 (d). The windshield was uniformly covered with relatively thin ice. Interestingly, most of the ice accumulated in the upper pylon. Thick ice was formed on the tail boom (x=1.4) where the high-speed rotor wakes collided, as shown in Figs. 7 (d) and 9. The thick ice region on the tail boom found in the hovering case moved further downstream as the wake shifted by the skew angle in low-speed cases.

The quantitative data on ice thickness at the mid-sectional plane of the fuselage at different locations such as nose, engine intake, and tail region are also shown in Fig. 8 for each case of the advance ratios. The mass of ice accretion near the nose region was observed to be the highest in the highest speed case with an advance ratio of 0.2 and almost negligible for hovering. In general, the thickness of ice at the same location was observed to decease with decreasing forward flight speed. The maximum ice thickness at the mid-section of the nose region was approximately 1.5 centimeters. The similar trend was found for ice accretion at the engine intake where ice accretion decreases with decreasing forward flight speed. The maximum ice thickness at the mid-section of the engine intake was approximately 1.1 centimeters. At the tail region, the maximum amount of ice accretion was observed for hovering and the amount of ice accretion decreased with increasing advance ratio. The maximum ice thickness at the mid-section of the tail region was approximately 0.55 centimeters. In summary, in the highest speed case with an advance ratio of 0.2 thick ice accumulated near the nose (x<0.1) and the engine intake (x=0.4). A dramatic increase in ice accretion was also observed on the windshield (0.1<x<0.2).

(a)

(b)

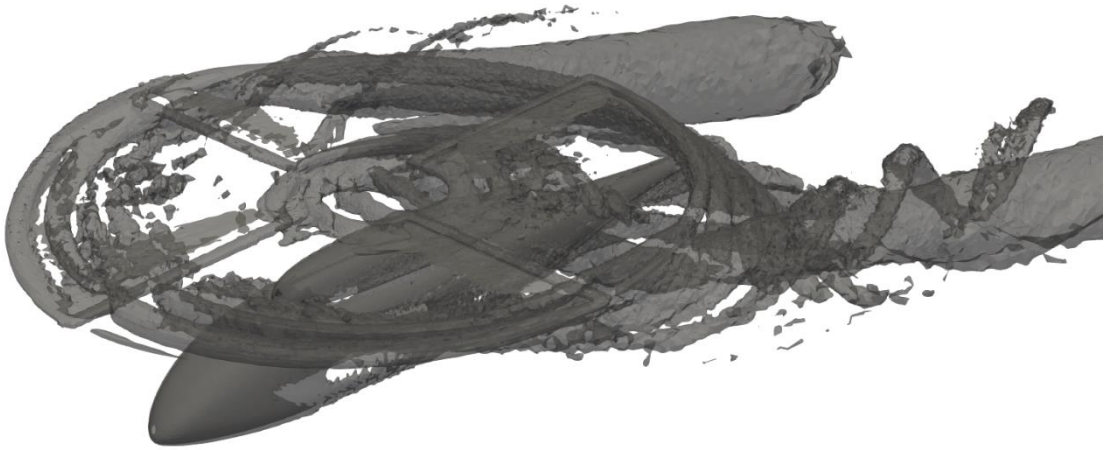

(c)

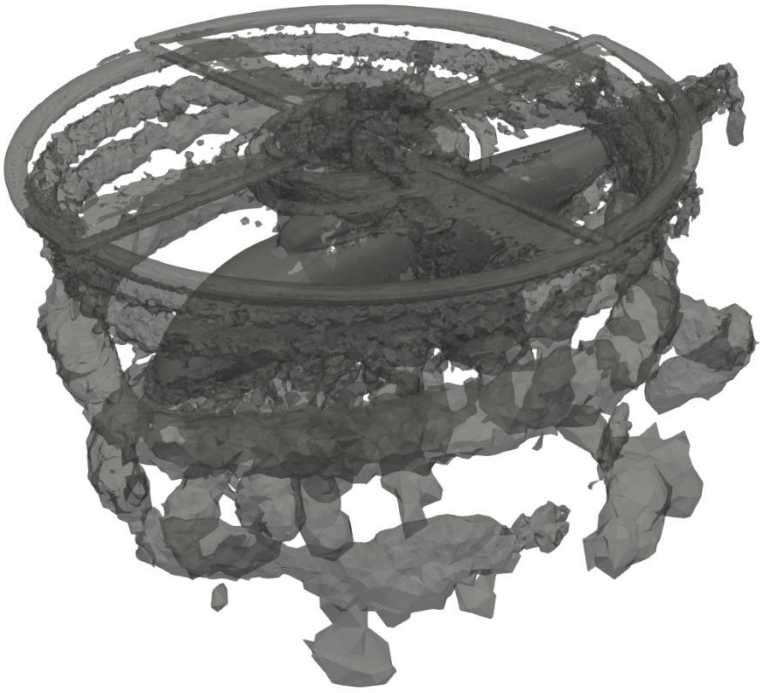

(d)

Fig. 7. Visualization of rotor wakes using Q-criteria (Q=1000) with various forward flight speeds; (a) μ=0.2, (b) μ=0.15, (c) μ=0.075, and (d) hovering.

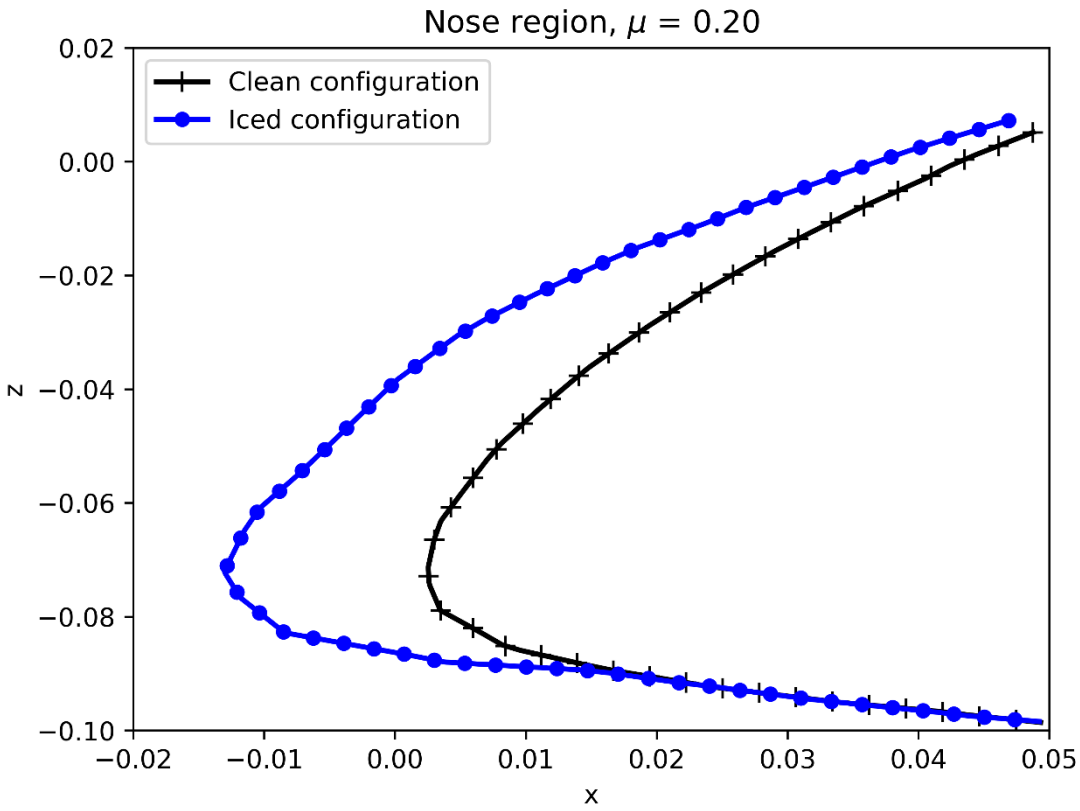
Nose region, μ = 0.20
Clean configuration
Iced configuration
0.02
0.00
−0.02
−0.04
−0.06
−0.08
−0.10
z
−0.02
−0.01
0.00
0.01
0.02
0.03
0.04
0.05
x

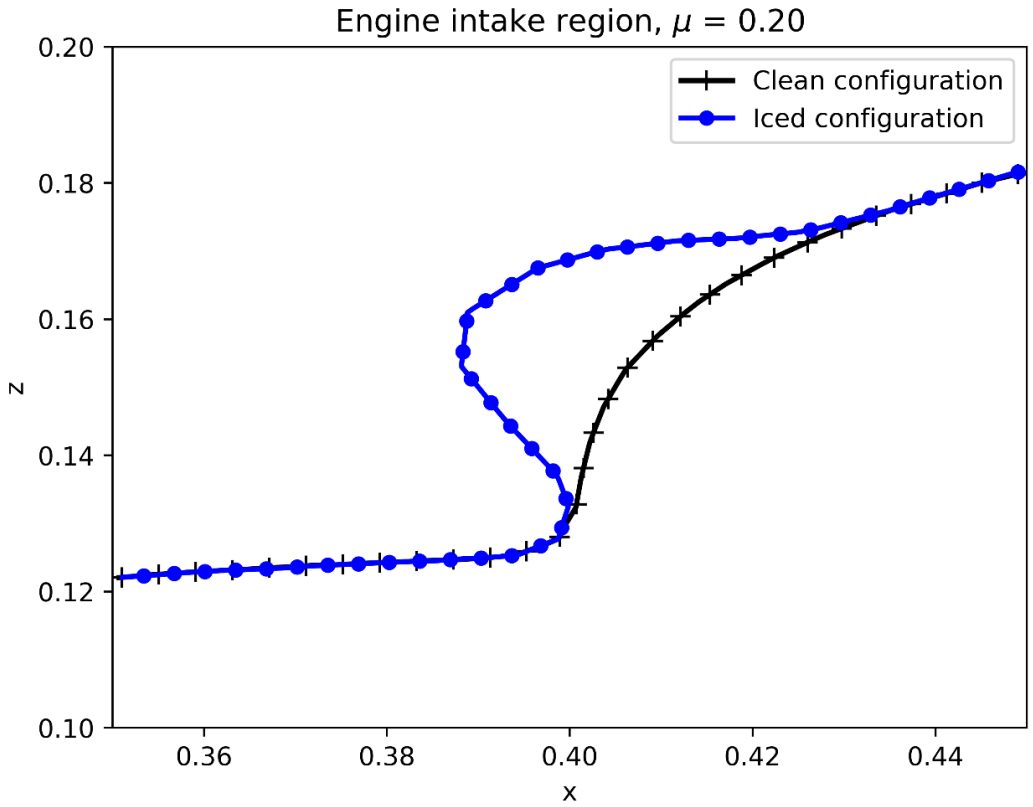
Engine intake region, μ = 0.20
Clean configuration
Iced configuration
0.20
0.18
0.16
0.14
0.12
0.10
z
0.36
0.38
0.40
0.42
0.44
x

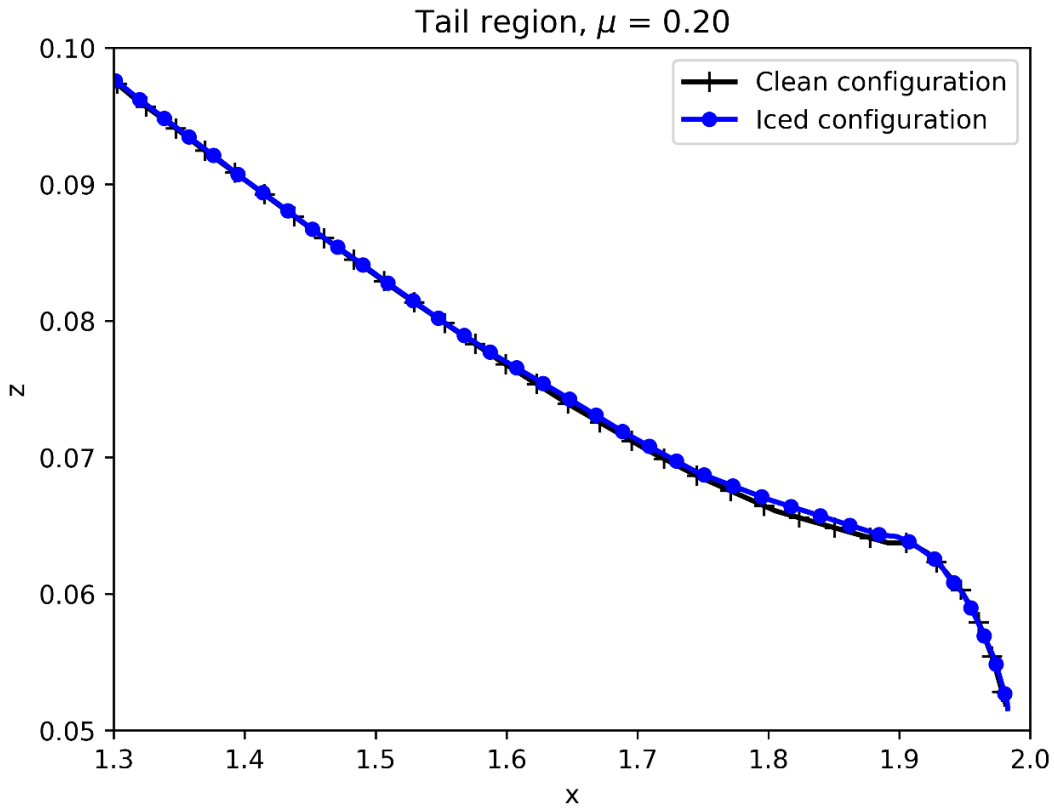
Tail region, μ = 0.20
Clean configuration
Iced configuration
0.10
0.09
0.08
0.07
0.06
0.05
z
1.3
1.4
1.5
1.6
1.7
1.8
1.9
2.0
x

(a)

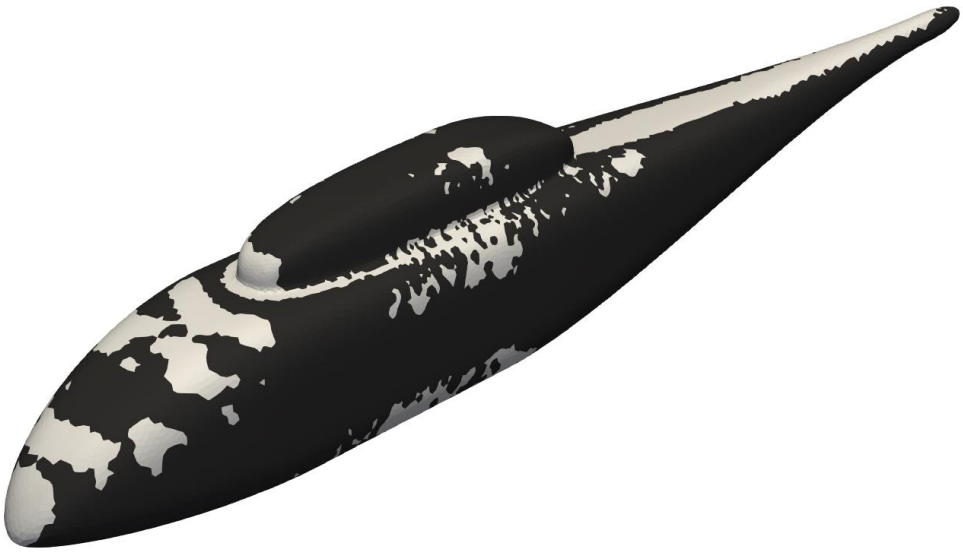

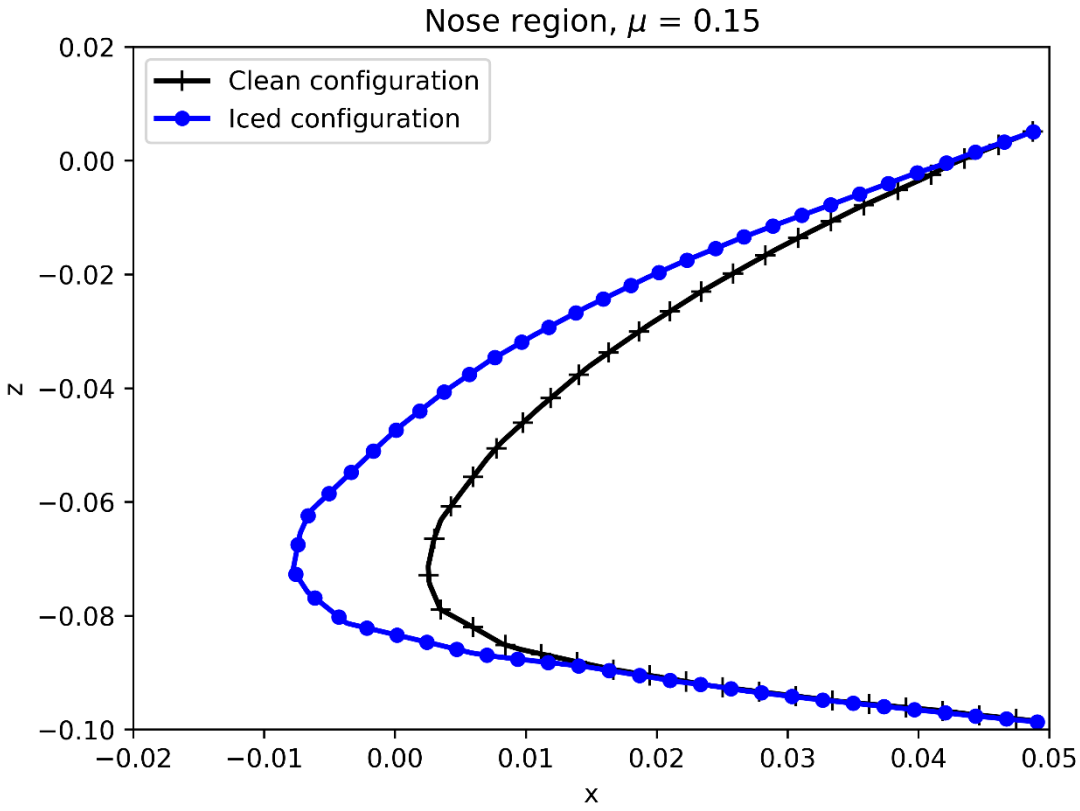
Nose region, $\mu = 0.15$
Clean configuration
Iced configuration
0.02
0.00
−0.02
−0.04
−0.06
−0.08
−0.10
z
−0.02
−0.01
0.00
0.01
0.02
0.03
0.04
0.05
x

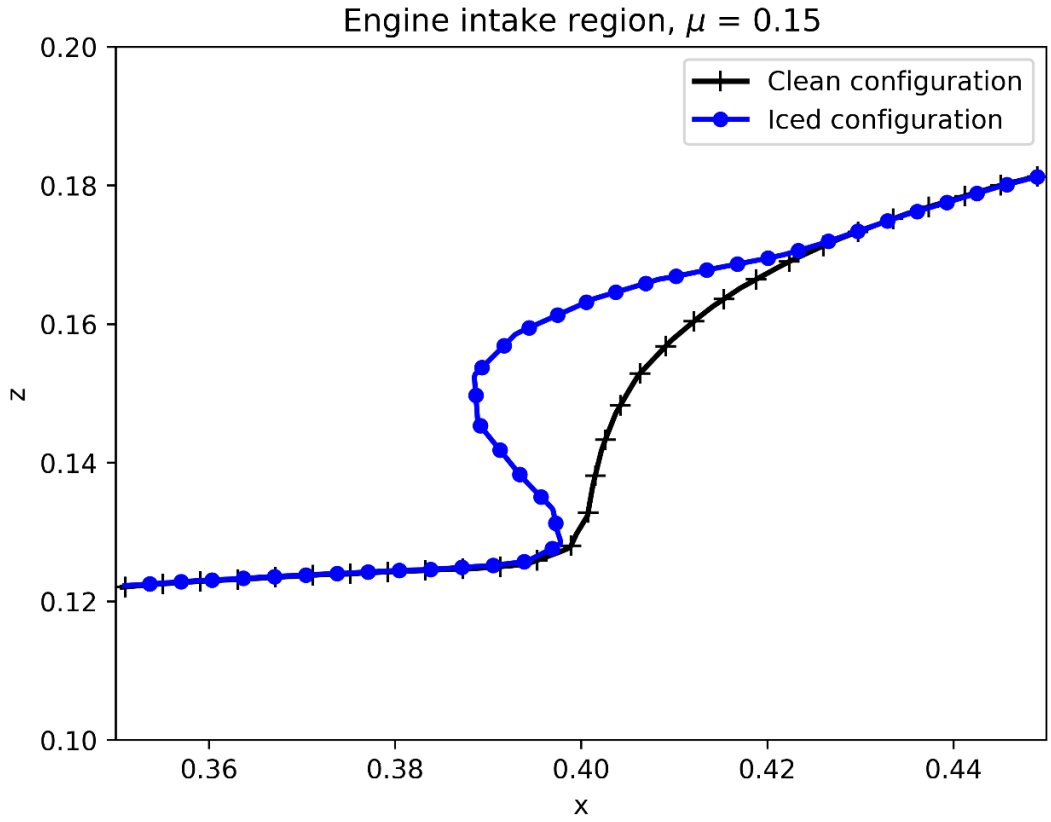
Engine intake region, μ = 0.15
Clean configuration
Iced configuration
0.20
0.18
0.16
0.14
0.12
0.10
z
0.36
0.38
0.40
0.42
0.44
x

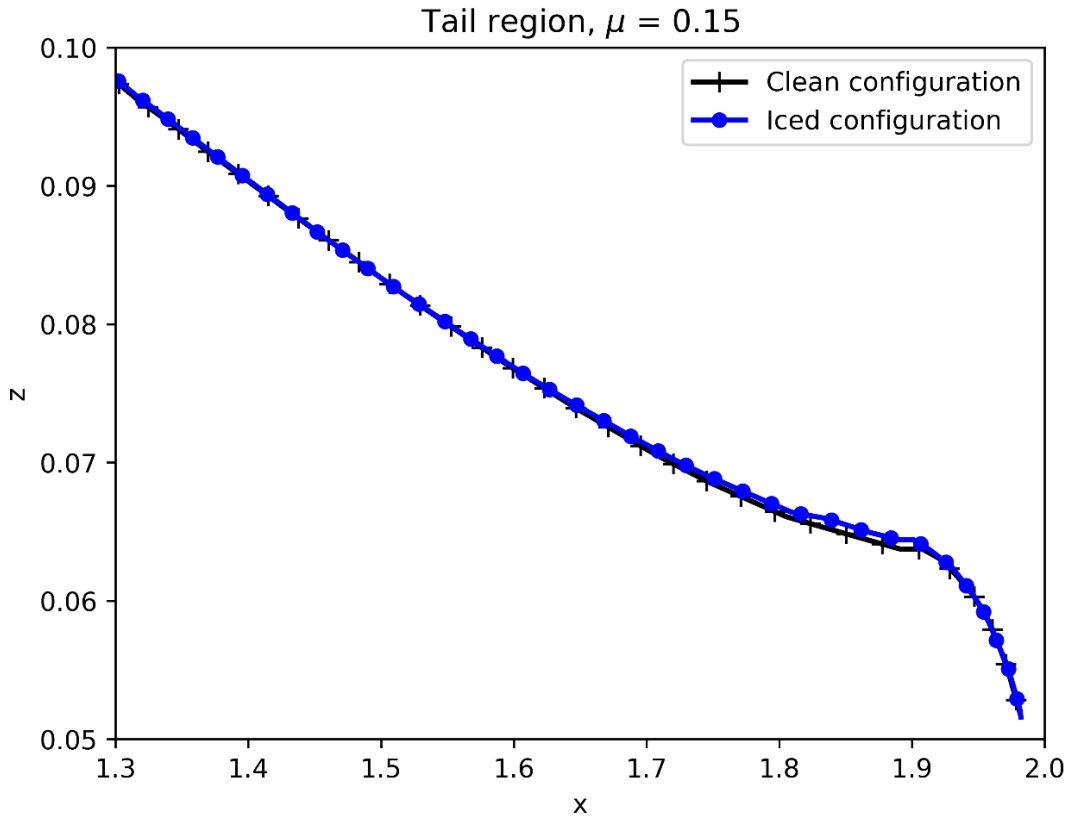
Tail region, μ = 0.15
Clean configuration
Iced configuration
0.10
0.09
0.08
0.07
0.06
0.05
z
1.3
1.4
1.5
1.6
1.7
1.8
1.9
2.0
x

(b)

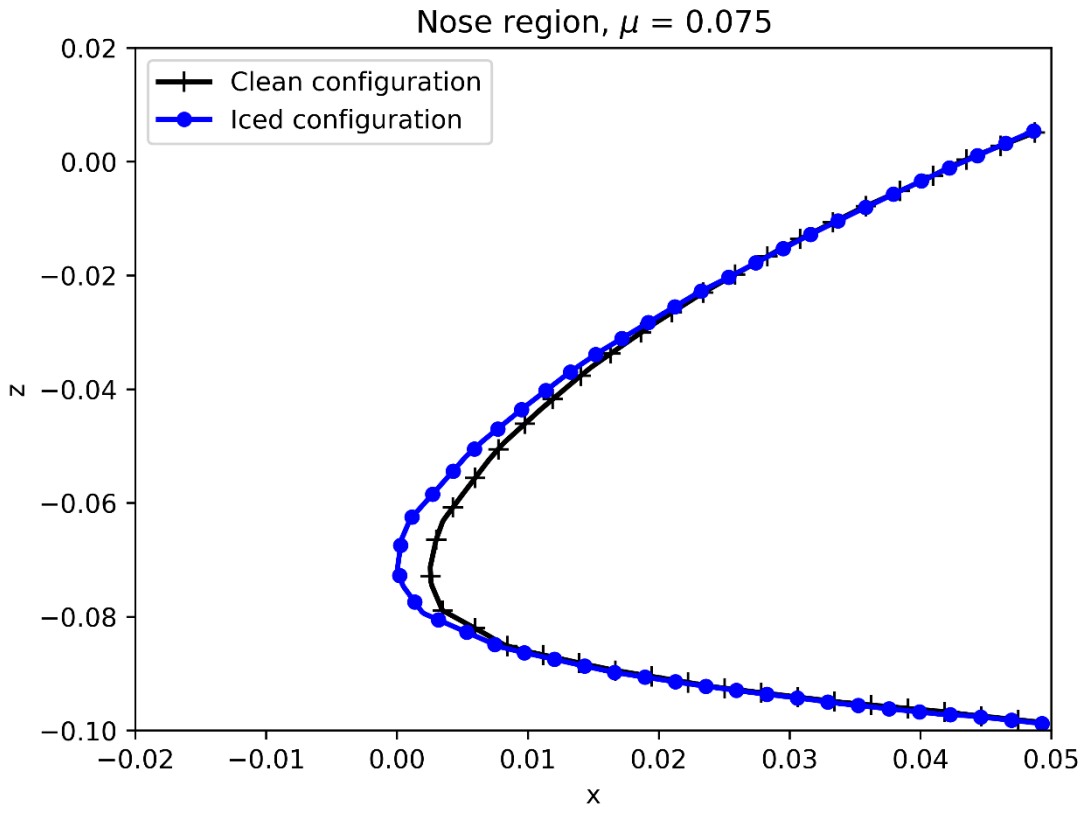
Nose region, μ = 0.075
Clean configuration
Iced configuration
0.02
0.00
−0.02
−0.04
−0.06
−0.08
−0.10
z
−0.02
−0.01
0.00
0.01
0.02
0.03
0.04
0.05
x

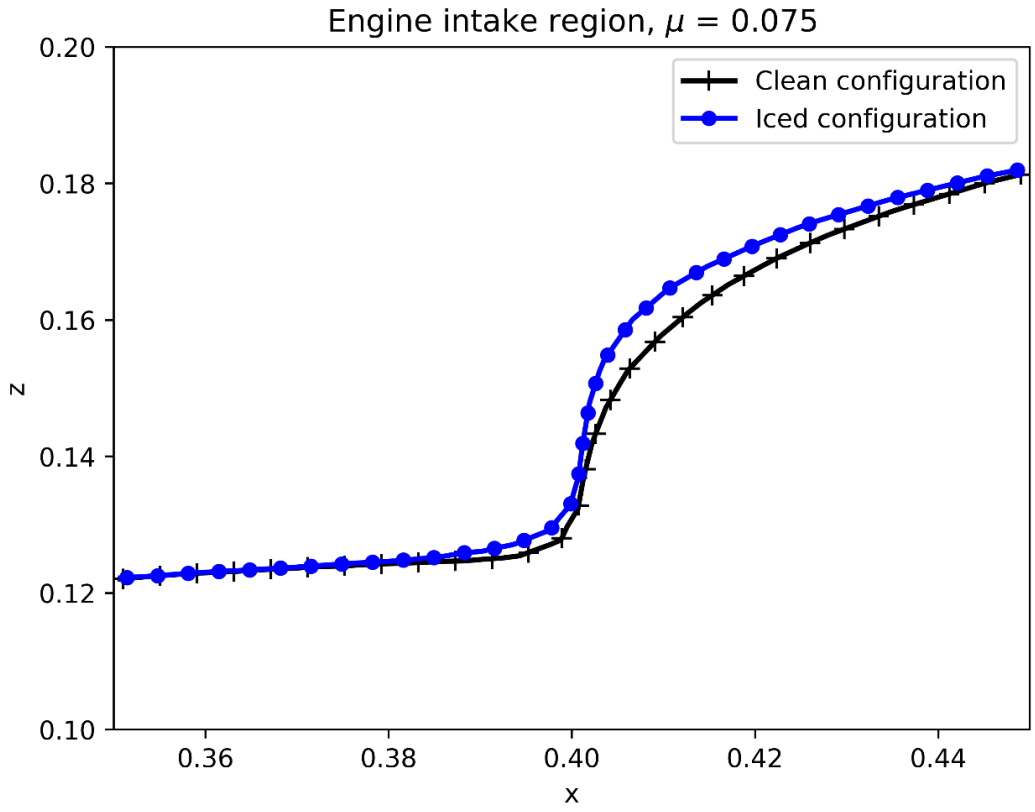
Engine intake region, μ = 0.075
Clean configuration
Iced configuration
0.20
0.18
0.16
0.14
0.12
0.10
z
0.36
0.38
0.40
0.42
0.44
x

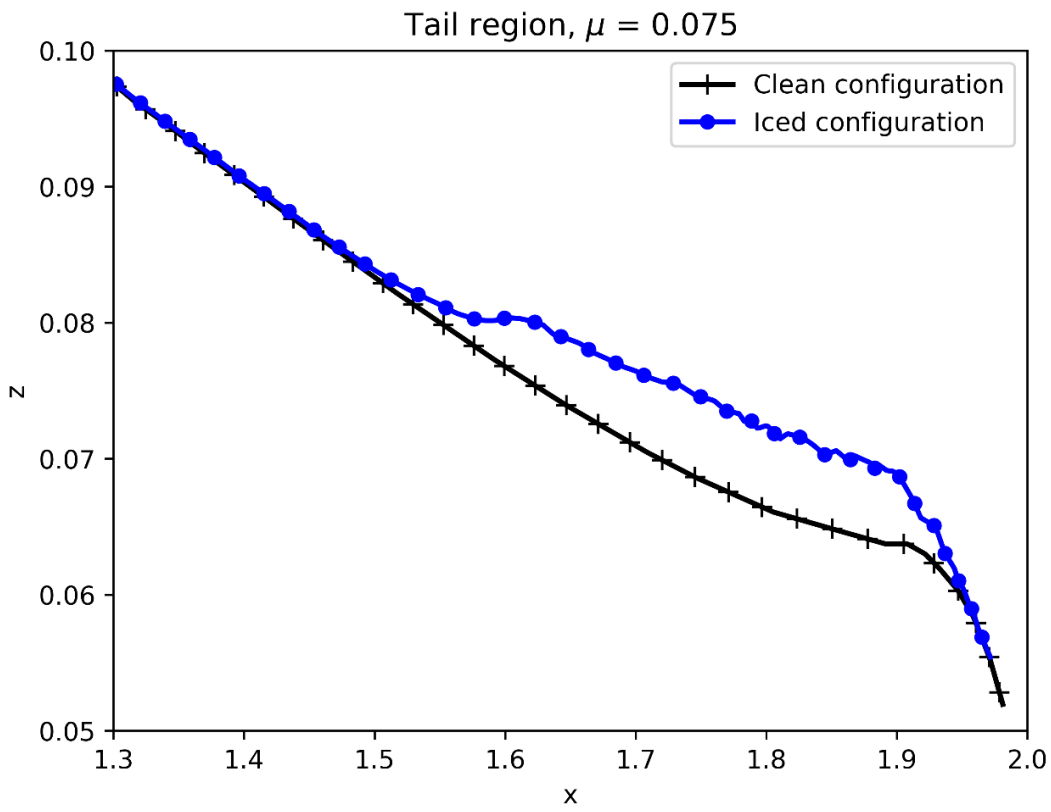
Tail region, μ = 0.075
Clean configuration
Iced configuration
0.10
0.09
0.08
0.07
0.06
0.05
z
1.3
1.4
1.5
1.6
1.7
1.8
1.9
2.0
x

(c)

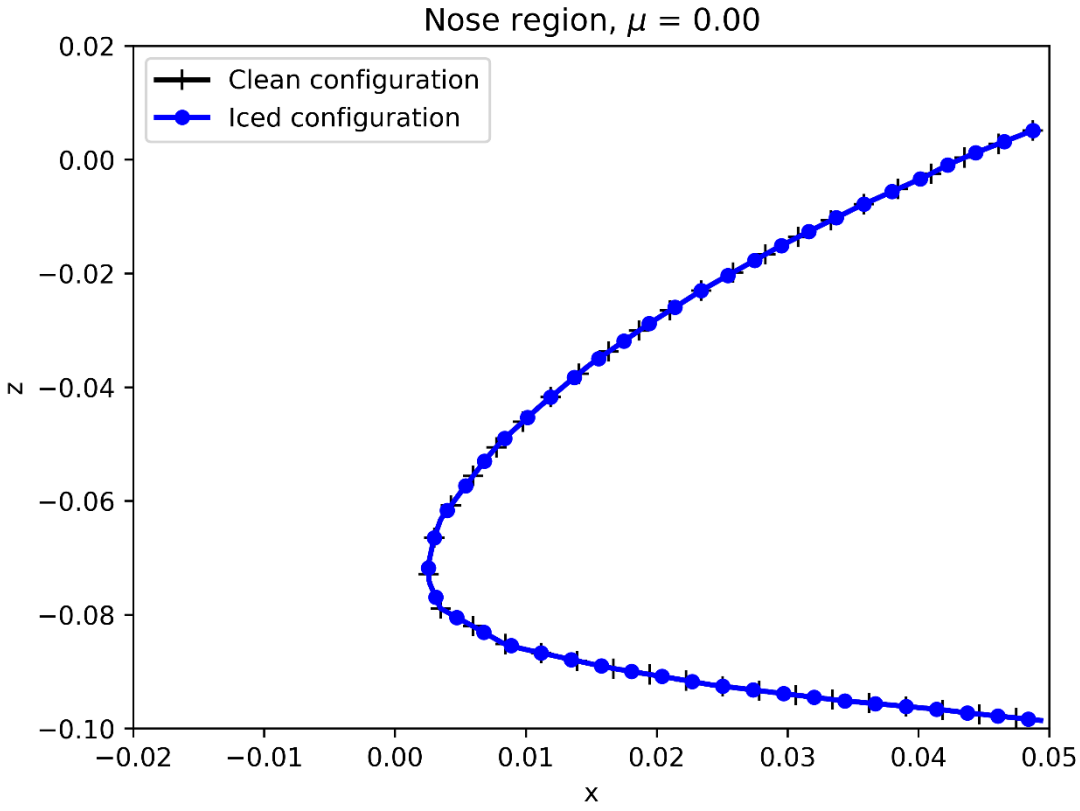
Nose region, μ = 0.00
Clean configuration
Iced configuration
0.02
0.00
−0.02
−0.04
−0.06
−0.08
−0.10
z
−0.02
−0.01
0.00
0.01
0.02
0.03
0.04
0.05
x

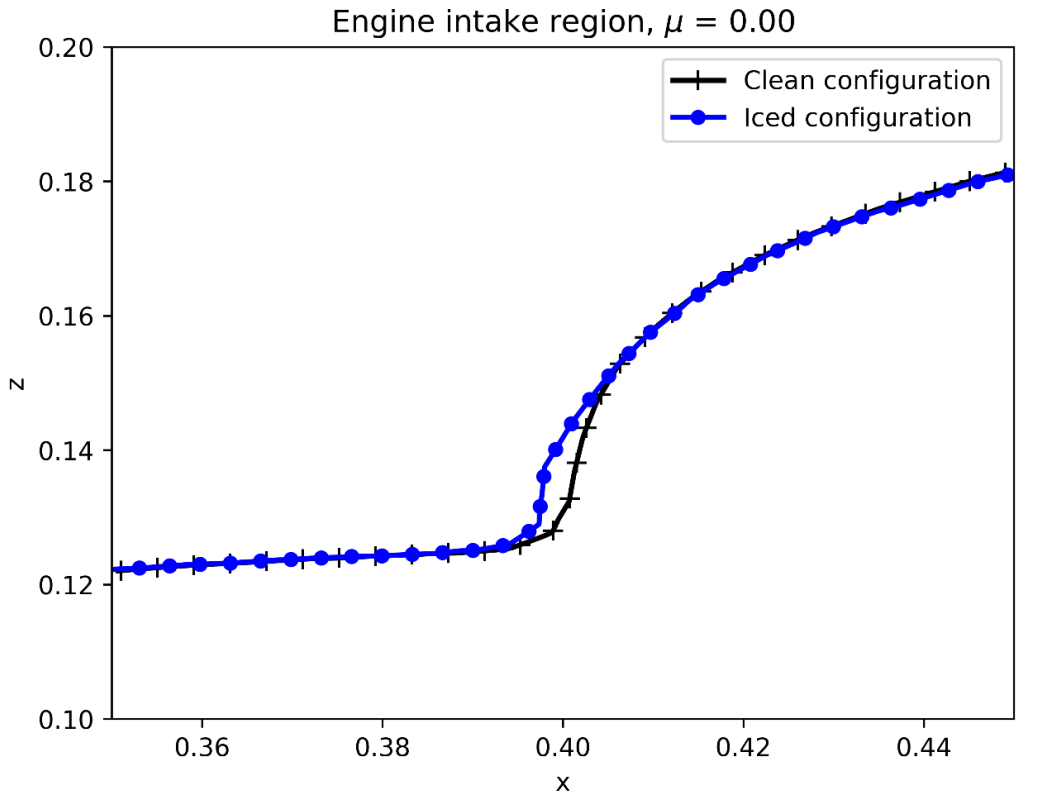

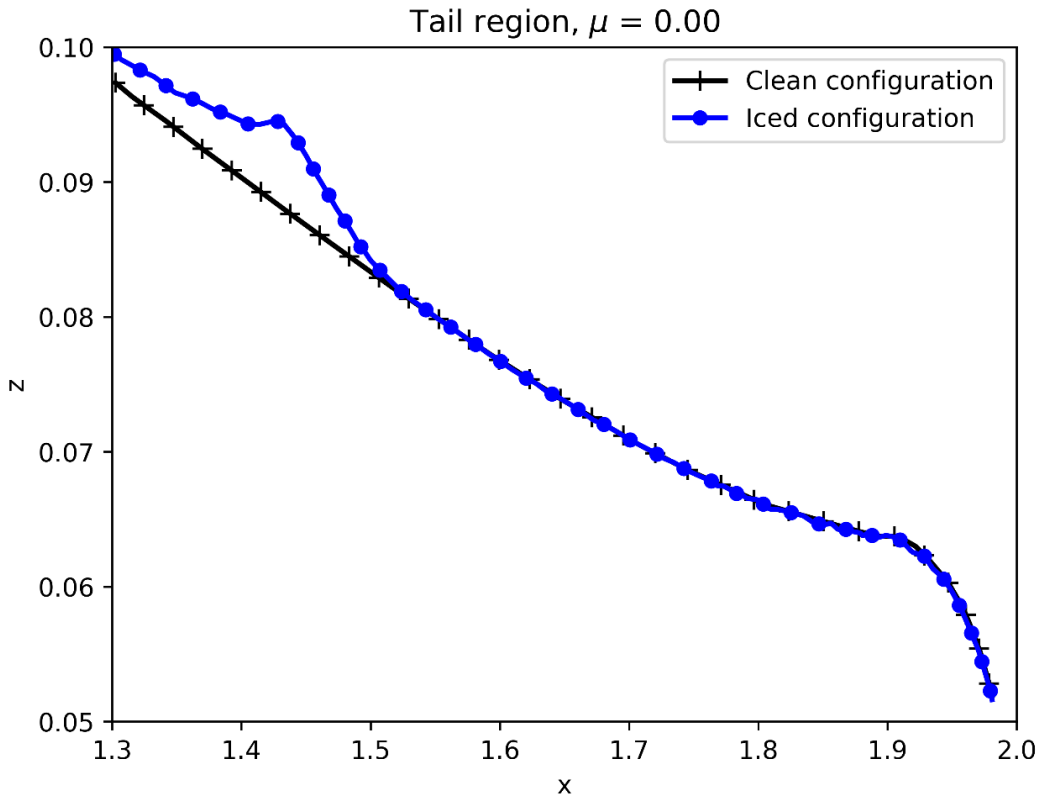

(d)

Fig. 8. Ice accretion shapes on the fuselage with mid-sectional view of ice thickness at nose, engine intake, and tail region for various forward flight speeds; (a) μ=0.2, (b) μ=0.15, (c) μ=0.075, and (d) hovering.

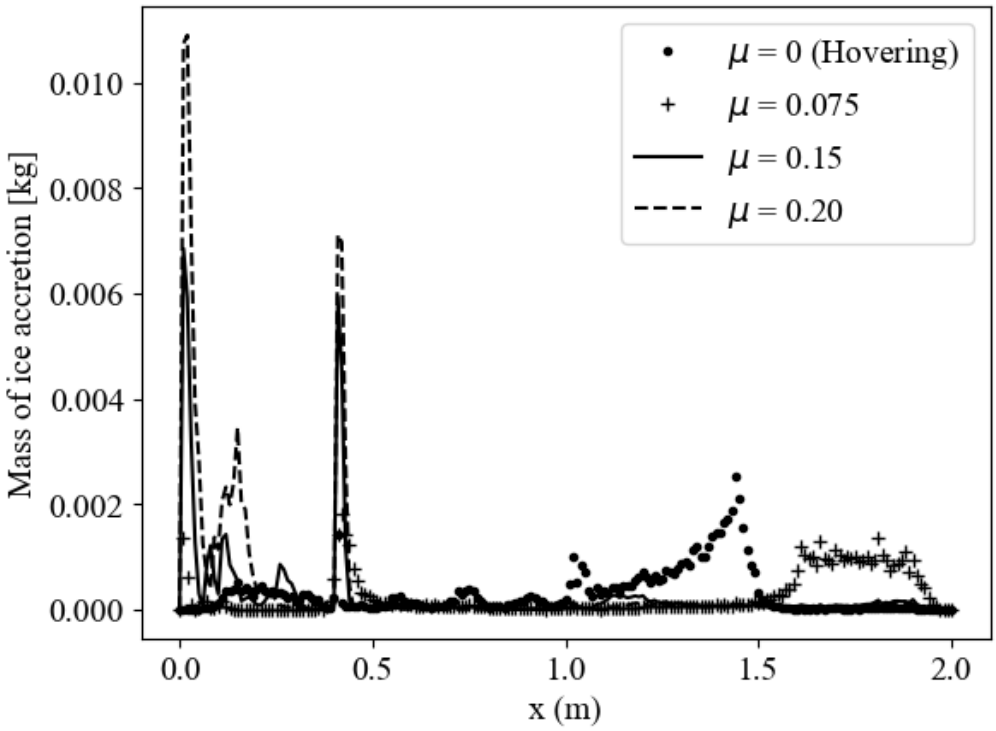

Fig. 9. Mass distribution of ice (in kilogram) accreted on the fuselage along the longitudinal direction. The horizontal coordinates x=0, 2 represent the nose and tail of the fuselage, respectively.

3.2. Grid independence study of a CFD code in generating aerodynamic database

The aerodynamic databases are required during the trajectory calculation because they provide the forces and moments acting on the ice fragments with respect to Euler angles. The aerodynamic database of the four shapes (plate, disc, ellipse, and GIS) were computed using an NSF-based CFD code for a combination of Euler angles. A mesh independence study was conducted to accurately evaluate the forces and moments in an optimal manner. Three different meshes, Mesh-1, Mesh-2, and Mesh-3, with the number of cells, 2,096,373, 2,822,981, and 5,294,179, respectively, were used for the study. Figure 10 shows the grid distribution around the rectangular flat plate (in Mesh-2) and the pressure coefficients on the surface of the plate for three different meshes. Since the difference between Mesh-2 and Mesh-3 was negligible, we selected Mesh-2 for further computations. The same rationale was applied to all other shapes when generating the aerodynamic database.

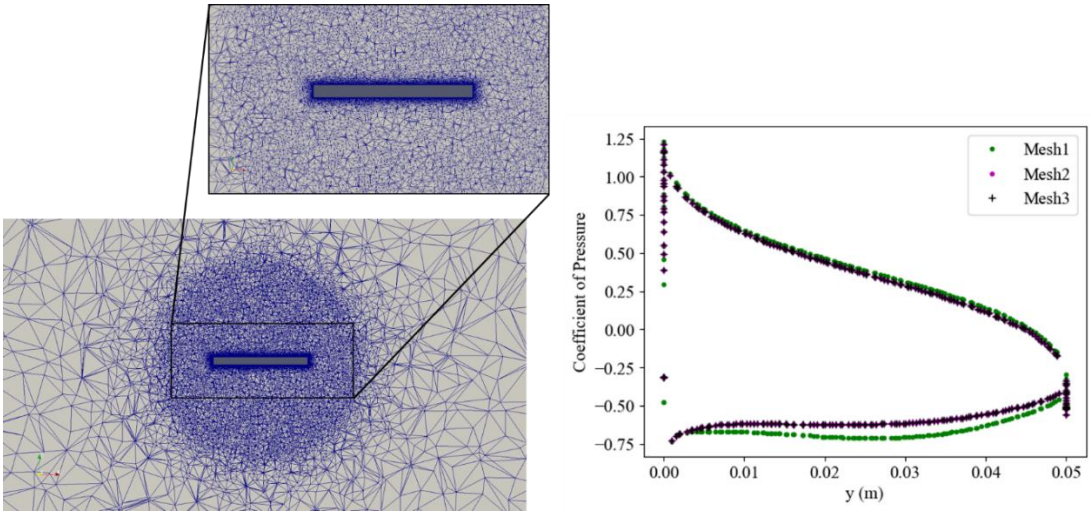

Fig. 10. Grid distribution around the plate (in Mesh-2) (left) and comparison of the pressure coefficients on the surface of the plate for three different meshes (right).

3.3. Verification and validation of the 6-DoF code

3.3.1. Verification of the 6-DoF code using analytical solutions

The first step in verifying a numerical code is to consider a case where a full analytical solution is available. Following this standard practice, we considered analytic solutions of the simplified equations of motion and compared them with the numerical results. For this purpose, we chose the rotation of the rectangular flat plate about the semi-major axis by an impulsively applied moment with the following conditions [74]:

$$\begin{aligned} &I_1 = 1, I_2 = 10, I_3 = 100, \\ &\omega_1 = 0, \omega_2 = 1, \omega_3 = 0. \end{aligned} \tag{12}$$

The system is subjected to an instantaneous perturbation by applying a moment along its minor axis: $M_1(0 \le t \le dt_1) = 0.01$. The analytical solution of angular velocities is given by the equations,

$$\begin{aligned}\omega_1 &= \pm 3.0151\,\mathrm{sech}(2.84605t),\\ \omega_2 &= \pm \tanh(2.84605t),\\ \omega_3 &= \pm 0.06534\,\mathrm{sech}(2.84605t).\end{aligned} \tag{13}$$

Figure 11 shows the undistinguishable numerical and analytical solutions, which alternate periodically due to the initial perturbation.

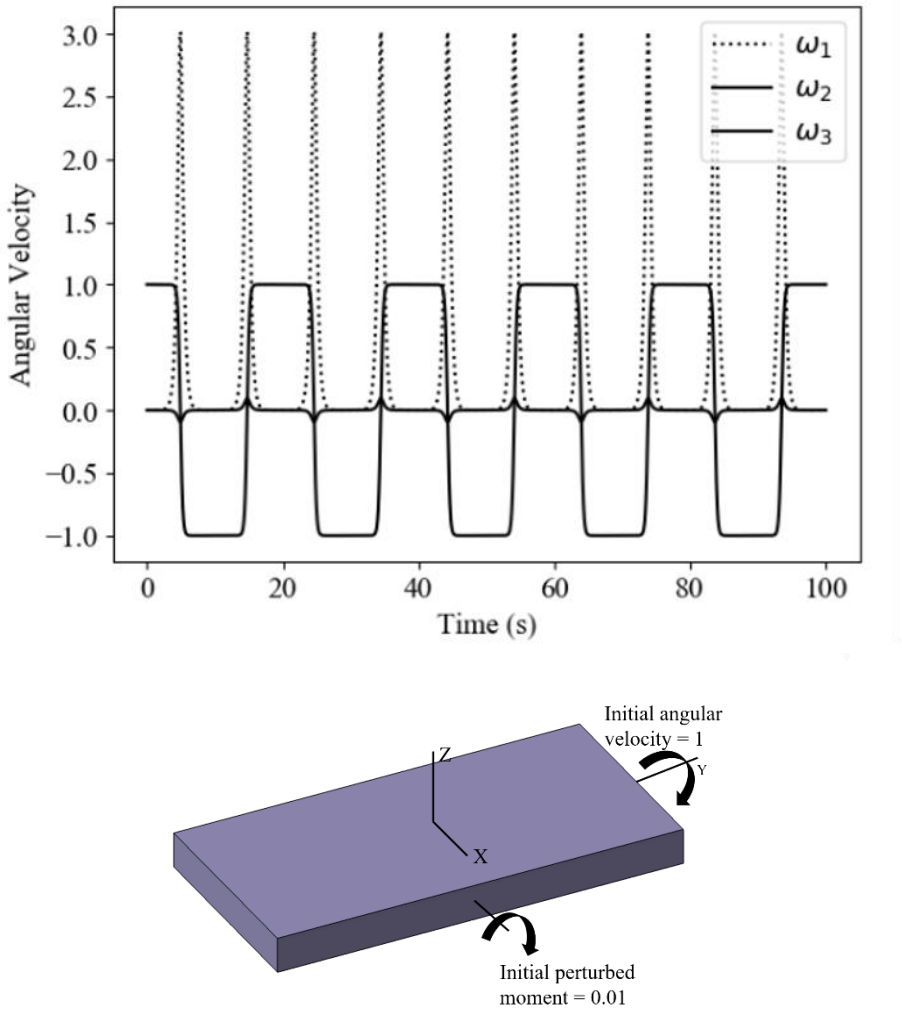

Fig. 11. Rotation of the rectangular flat plate about the semi-major axis perturbed by an impulsively applied moment.

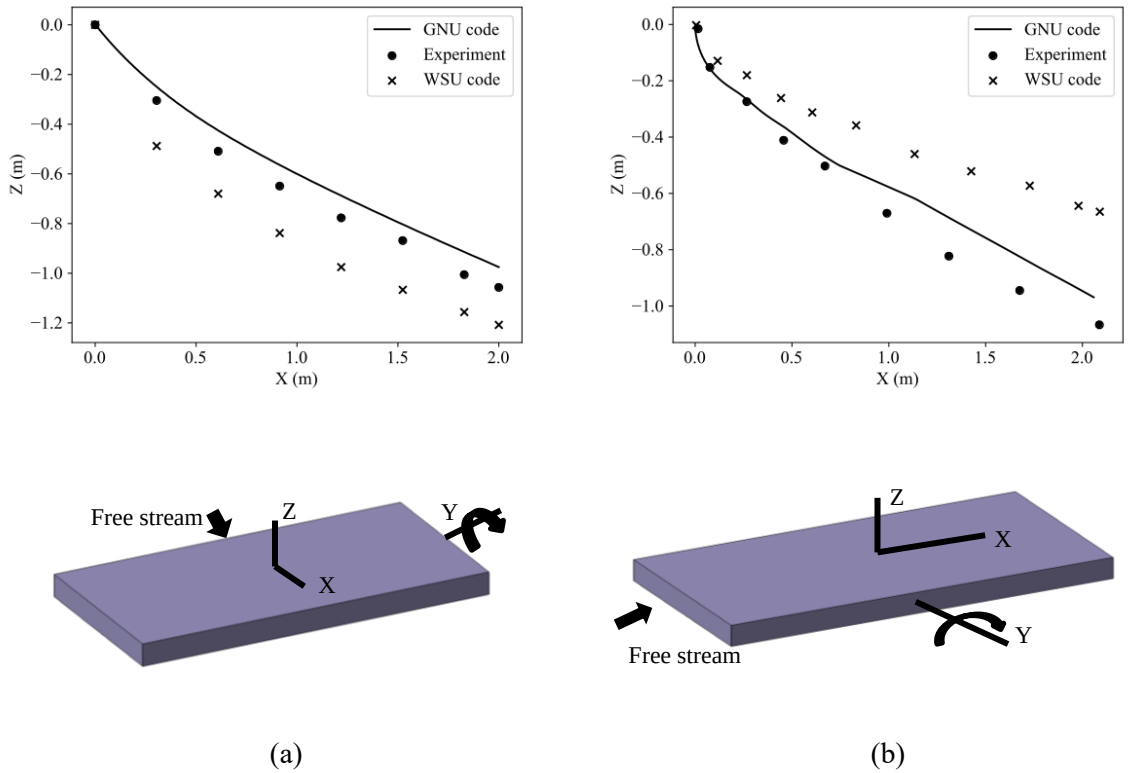

Fig. 12. Validation of the 6-DoF code for (a) RFP12 and (b) RFP6 configurations.

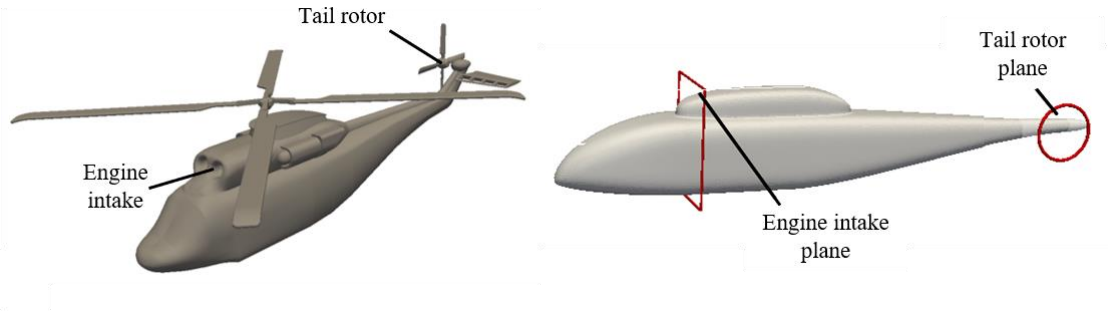

Fig. 13. Engine intake and tail rotor planes considered for the computation of footprint density and Monte Carlo probability density.

3.3.2. Validation of the 6-DoF code using wind tunnel test data

To validate the 6-DoF code for the realistic icing shedding problem with the underlying airflow field, we selected a wind tunnel test with two configurations of rectangular flat plate (RFP), RFP12 and RFP6, conducted by Wichita State University (WSU) [23]. The wind tunnel test was conducted with a wind velocity of approximately 70 meters per second. The inertial frame of reference was fixed on the wind tunnel with the X-axis being in the direction of the flow, the Z,Y-axes being perpendicular in the vertical and horizontal directions, respectively, with respect to the X-axis, as illustrated in Fig. 12. The trajectories were extracted from high-speed video images using the grids attached to the tunnel ceiling and sidewall. The trajectory distance recorded in the tests ranged from approximately 2.0 to 2.2 meters. The RFP12 and RFP6 configurations were released with zero angles of attack in the wind tunnel. Figure 12 compares the trajectories of the WSU wind tunnel test, WSU 6-DoF code, and the present 6-DoF code, for the RFP12 and RFP6 configurations. The trajectory computed by the present 6-DoF code closely follows the test data of the WSU wind tunnel.

3.4. Trajectory analysis and Monte Carlo simulation of the engine intake and tail rotor planes

We conducted trajectory analysis and Monte Carlo simulations for four representative ice shapes: plate, disc, ellipse, and GIS. Each type of shed ice was traced from their shedding locations to a point where the trajectory passed through the vertical plane formed by the intersection of the engine intake, as shown in Fig. 13. The same procedure was applied to the plane of the tail rotor. The intersection of the shed ice trajectories and the engine intake or tail rotor planes is called the trajectory footprint.

We selected four main parameters—forward flight speed, break-off location, ice shape, and the Euler angles (roll, pitch, and yaw)—and treated the Euler angles randomly in 6-DoF simulations. Initial ice break-off locations were chosen based on information about ice accretion on the surface, and the study of the criticality of break-off locations. Each of these locations was tested with a hundred trajectory computations for different sets of randomly generated initial Euler angles. Ice fragments shed from most of these locations were not able to reach the engine intake

plane or the tail rotor plane, because the trajectory was way off the planes. In a few other cases, ice was not able to reach the engine intake plane, since it collided with the helicopter surface before it could reach the engine intake plane. After considerable trajectory computations, we identified five representative break-off locations, shown in Fig. 5, and considered them for all following calculations. After selecting the break-off locations, we repeated the trajectory computations for randomly chosen Euler angles (initial orientation) with four different ice shapes. The outcomes from the 6-DoF simulations were used to train the neural network.

The trajectory data obtained from the trained neural network were then utilized to generate the input for the Monte Carlo simulations. The total number of trajectory footprints at the engine intake plane was always less than the number of shed ice, since a specific combination of initial Euler angles will result in trajectories which collide with the helicopter surface before reaching the engine intake plane or the tail rotor plane. A trajectory footprint density map and Monte Carlo probability density map were then computed from the neural network and Monte Carlo simulation, respectively. The footprint density indicates the number of ice fragments hitting the location per unit area for a discrete set of events. On the other hand, the Monte Carlo probability represents the probability of hitting for numerous random events spread over the variable space associated with the phenomenon of ice shedding. The location of the engine intake and tail rotor planes is shown in Fig. 13.

3.4.1. Footprint analysis on the engine intake plane

We first investigated the footprint density and Monte Carlo probability density on the engine intake plane for different flow fields, initial break-off locations, and ice shapes.

Effect of flow conditions

To investigate the effect of flow conditions on footprint density and Monte Carlo probability density in the rotorcraft flow field, we performed 6-DoF simulations for different advance ratios: 0.2, 0.15, 0.075, and 0.0 (hovering). The density maps for each flow condition were obtained by randomly varying initial orientations (Euler angles) and, at the same time, by considering various

combination of initial break-off locations and ice shapes. Figure 14 shows that the footprint density and Monte Carlo probability density on the engine inlet plane increased with increasing advance ratio. On the other hand, it turned out that there was no footprint in case of hovering, owing to the strong downwash and its effect of blocking ice fragments approaching the engine intake plane. For this reason, the density maps were not presented.

As the advance ratio increased, the velocity in the flow field also increased. Since the aerodynamic forces and moments acting on the ice fragment are proportional to the square of the relative velocity, the ice fragments experience higher force both in the downstream and upward directions. The force in the downstream direction helps the ice fragment to move in the same direction. In contrast, the force in the upward direction lifts the ice fragment and makes the situation more dangerous. As the flight speed increases, the direction of the downwash moves towards the downstream direction with an increased wake-skew angle, which assists in carrying the ice fragment with the airflow. Based on the maps of footprint density and Monte Carlo probability density, high-speed flight in icing conditions makes it more likely that ice fragments will hit the engine intake plane, than low-speed flight.

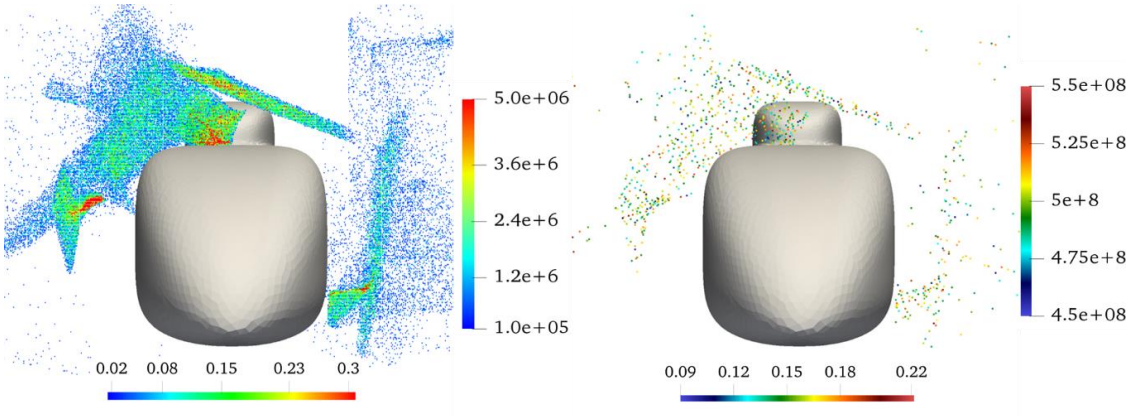

(a)

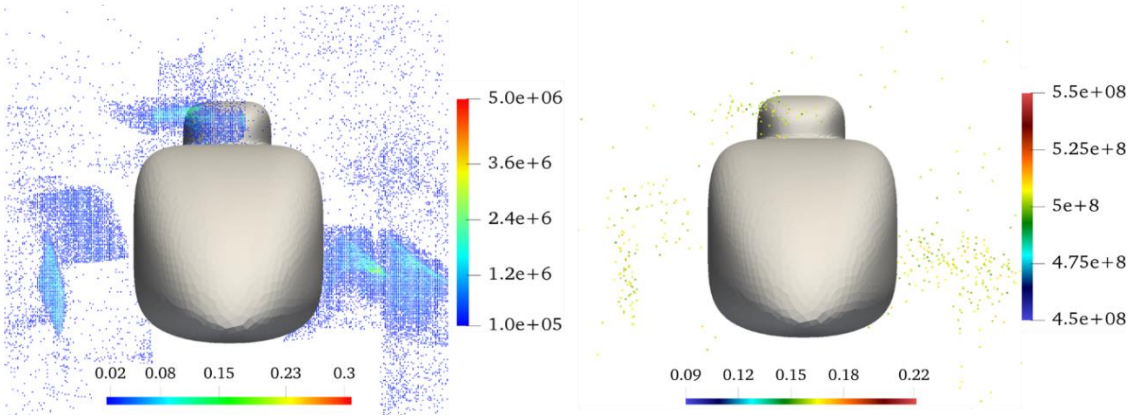

(b)

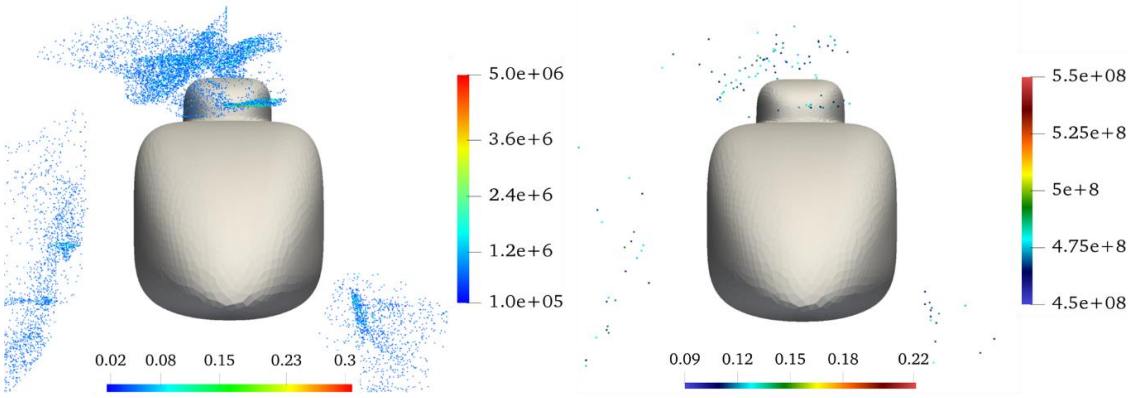

(c)

Fig. 14. Footprint density (left) and Monte Carlo probability density (right) for different advance ratios: (a) μ=0.2, (b) μ=0.15, and (c) μ=0.075. The vertical numbers represent the actual hits, while the horizontal numbers represent the corresponding percentage.

Effect of initial break-off locations

We repeated the 6-DoF simulations to investigate the effect of initial break-off locations on footprint density and Monte Carlo probability density. Like the previous case, the density maps were obtained by randomly varying initial orientations (Euler angles) and, at the same time, by considering various combination of flow conditions and ice shapes.

Location A is located at the centerline, which makes it relatively closer to the engine intake plane than other break-off locations. As a result, a large number of ice fragments not only hit the engine intake plane, but a significant percentage of ice fragments also hit the engine intake itself, as shown in Fig. (a).

To understand the footprint pattern of the off-centered break-off locations (B-E), it is vital to consider the direction of the rotation of the main rotor blade. As the rotor blade rotates counterclockwise (viewed from the top), the vortex generated by the rotor blade tends to collide with the left side (viewed from the front) of the fuselage. As a consequence, the initial break-off locations B and C encounter an inward flow towards the center of the fuselage. The ice fragment shed from B has a greater chance of reaching the engine intake plane and the actual engine intake than that shed from C, as shown in Fig. 15 (b) and (c), since B is located closer to the engine intake plane than C.

On the other hand, the initial break-off locations D and E experience an outward flow, since they are located on opposite sides of the fuselage. As a result, ice fragments shed from D and E tend to move away from the fuselage, as shown in the Fig. 15 (d) and (e).

In summary, the direction of the main rotor blade contributes significantly to the trajectory footprint, which is quite different from the case of fixed-wing aircraft, making computation of ice shedding trajectories on rotorcraft with strong rotor wakes very complicated.

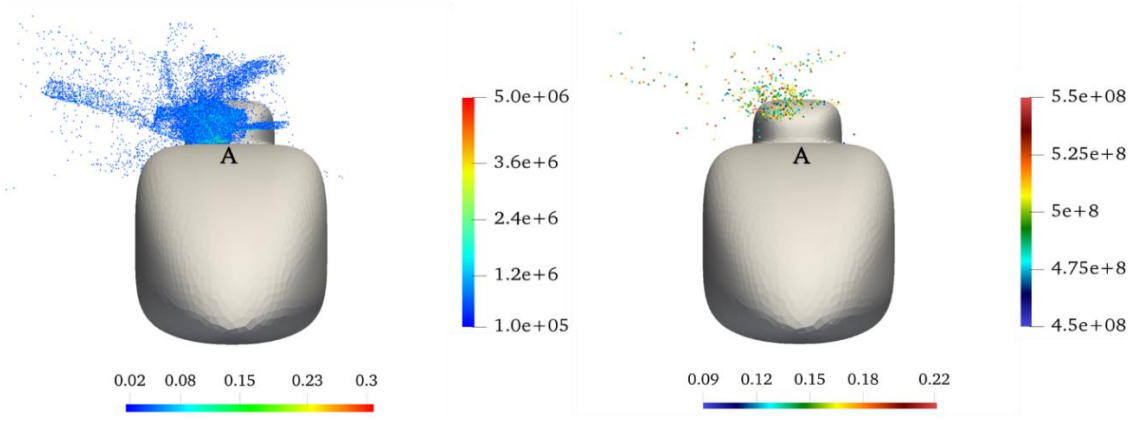
A
5.0e+06
3.6e+6
2.4e+6
1.2e+6
1.0e+05
0.02 0.08 0.15 0.23 0.3
A
5.5e+08
5.25e+8
5e+8
4.75e+8
4.5e+08
0.09 0.12 0.15 0.18 0.22

(a)

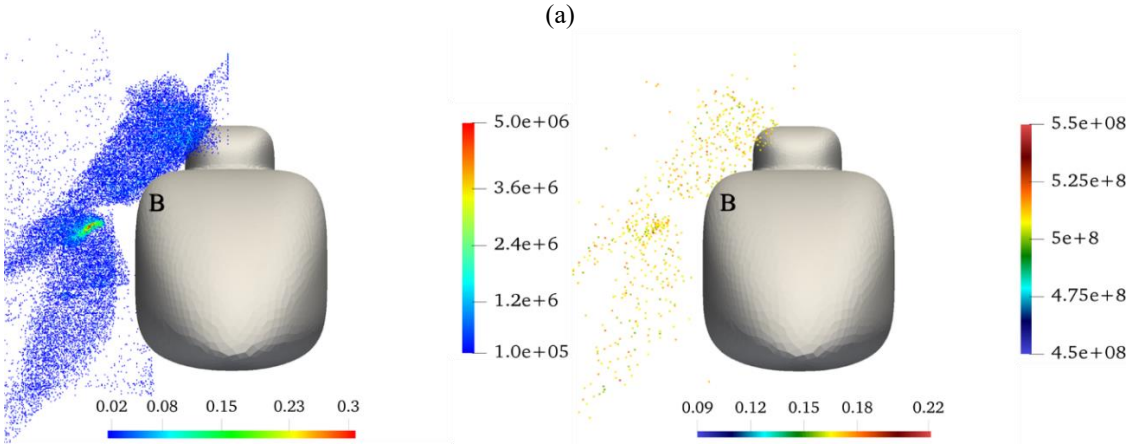
B
5.0e+06
3.6e+6
2.4e+6
1.2e+6
1.0e+05
0.02 0.08 0.15 0.23 0.3
B
5.5e+08
5.25e+8
5e+8
4.75e+8
4.5e+08
0.09 0.12 0.15 0.18 0.22

(b)

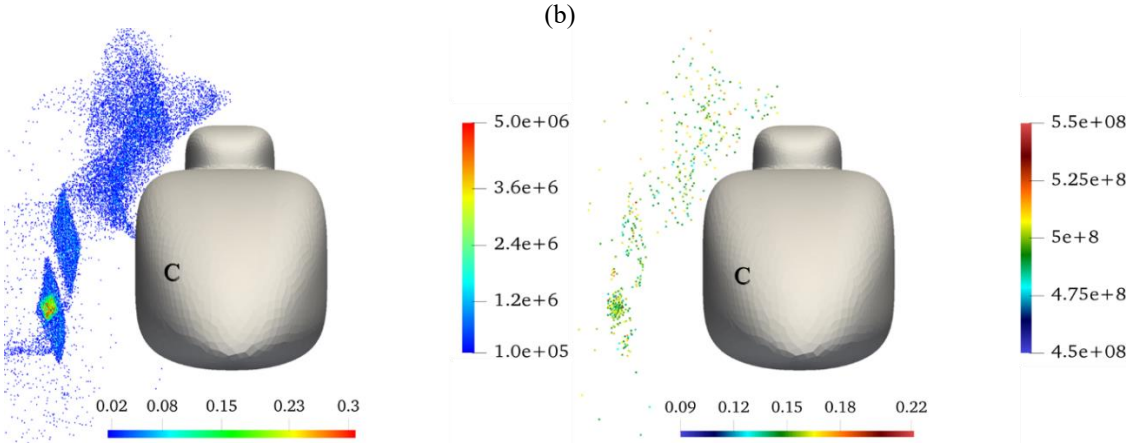
C
5.0e+06
3.6e+6
2.4e+6
1.2e+6
1.0e+05
0.02 0.08 0.15 0.23 0.3
C
5.5e+08
5.25e+8
5e+8
4.75e+8
4.5e+08
0.09 0.12 0.15 0.18 0.22

(c)

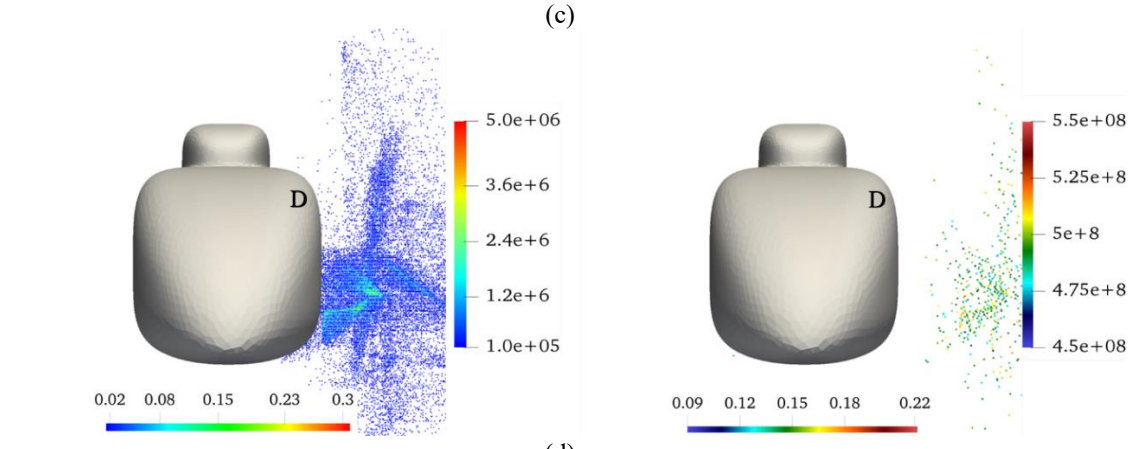
D
5.0e+06
3.6e+6
2.4e+6
1.2e+6
1.0e+05
0.02 0.08 0.15 0.23 0.3
D
5.5e+08
5.25e+8
5e+8
4.75e+8
4.5e+08
0.09 0.12 0.15 0.18 0.22

(d)

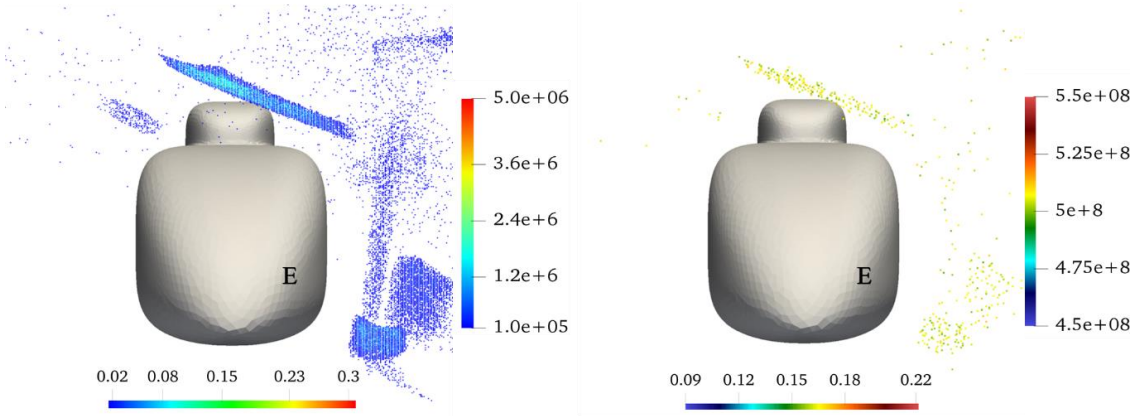

(e)

Fig. 15. Footprint density (left) and Monte Carlo probability density (right) for different initial break-off locations: (a) A, (b) B, (c) C, (d) D, and (e) E. The vertical numbers represent the actual hits, while the horizontal numbers represent the corresponding percentage.

Effect of ice shapes

The shape of the ice fragments may have a significant effect on footprint density and Monte Carlo probability density. The rationale for the representative ice shapes (plate, disc, ellipse, and GIS) was described in detail in Section 2.2. We repeated the 6-DoF simulations by randomly varying initial orientations (Euler angles) and, at the same time, by considering various combinations of flow conditions and initial break-off locations.

A further complication related to fundamental ice physics may come into play with the effect of ice shapes: the ice density. The density of ice in in-flight aircraft icing is not constant; rather, it depends on the meteorological conditions, the rate of ice formation, presence of foreign particles, and pores during freezing. To mimic the real physics, the ice density was randomly varied from 850 to 918 kg/m^3 [75,76] during simulations.

It is well known in aerodynamics that the shape of an object (like an ice fragment) has a significant impact on the magnitude of aerodynamic forces and moments that will be exerted on the object. Figure 16 shows the critical role of the ice shape in the footprint density and Monte Carlo probability density. The plate-shaped ice with sharp edges showed the highest footprint density on both sides of the fuselage at the engine intake plane, as shown in Fig. 16 (a). However,

those footprints are contained in compact regions located considerably away from the fuselage and the engine intake, making this type of ice shape least dangerous. In contrast, disc-shaped ice with a sharp edge was found to be the most dangerous, as shown in Fig. 16 (b).

The third kind of representative ice shape, elliptic shape ice with rounded edges, was found to be not very threatening, since the footprint density is very small and distributed uniformly at the engine intake plane, as shown in Fig. 16 (c). On the other hand, the GIS ice showed a pattern similar to the disc-shaped ice, but with much less density near the engine intake, making this type of ice shape less dangerous than the disc-shaped ice. The GIS ice is close to a realistic ice shape, with an asymmetric shape in all three axes and with the presence of local irregularities. Because of the local randomness in shape, the aerodynamic effect and the footprint pattern are less intuitive.

The unusually high footprint density of the disc-shaped ice at the engine intake can be explained as follows. The disc-shaped ice is geometrically symmetric along the roll and pitch axes. Because of this symmetry, the side force coefficient of the disc-shaped ice has a similar order of magnitude with the axial force coefficient. Although the normal and axial force coefficients of the plate-shaped ice have similar orders of magnitude as the disc-shaped ice, the side force coefficient of the plate-shaped ice is much lower than that of the disc-shaped ice. Therefore, when the ice is released from the off-centered break-off locations, because of the higher side force, disc-shaped ice fragments are more likely to reach near the engine intake than the plate-shaped ice. In contrast, the plate-shaped ice was unable to reach the engine intake, even when it was released from location A at the centerline and with a very high initial pitch angle (more than 80 degrees).

The type of edge of the ice fragments was found to be another factor that had a strong influence on the footprint patterns. The effect of edge type can be easily observed by comparing the footprints of the plate-shaped ice with sharp edges (Fig. 16 (a)) and the elliptic shape ice with rounded edges (Fig. 16 (c)). The difference is striking and is due to the aerodynamic effect: The fragment with sharp edges experiences smaller aerodynamic force than the fragment with rounded edges. As a result, the fragment with sharp edges experiences a higher acceleration in the vertical and downstream directions. Consequently, the footprints of the fragment with sharp edges are densely distributed in compact regions, while the footprints of the fragment with rounded edges

are widely spread over the engine intake plane.

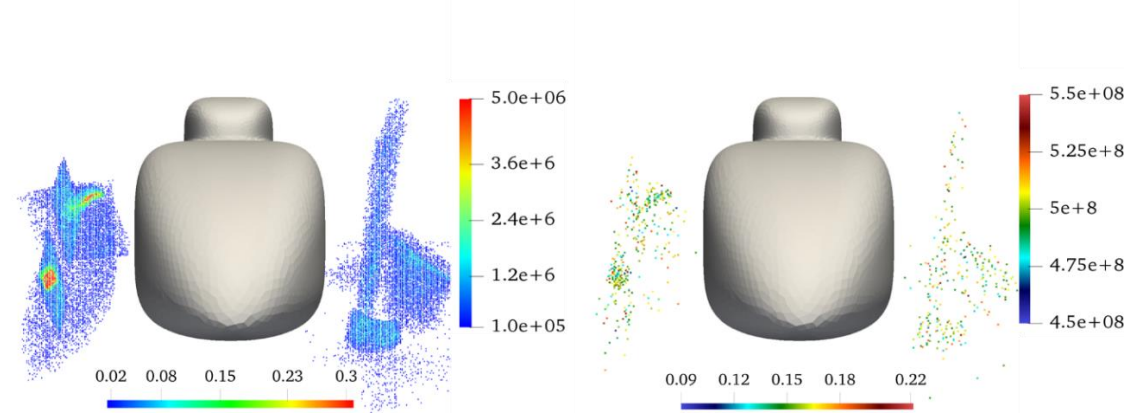

(a)

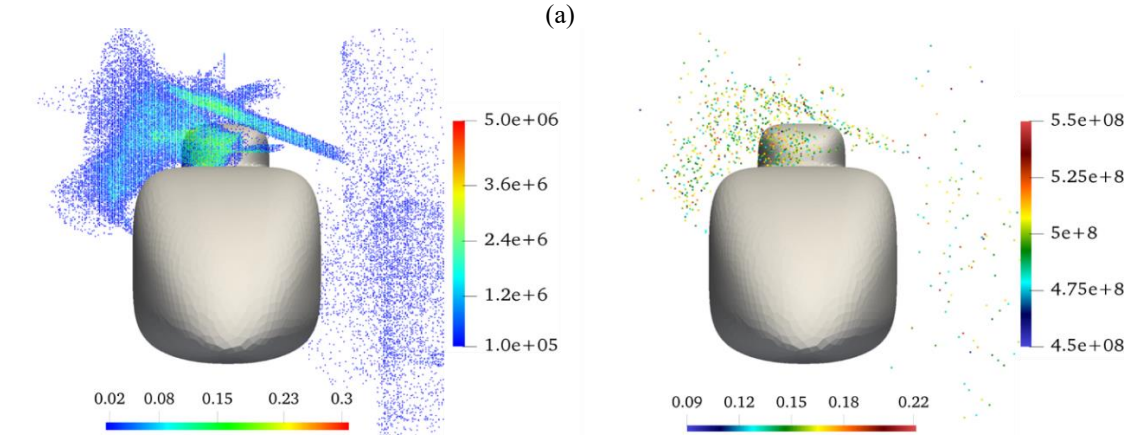

(b)

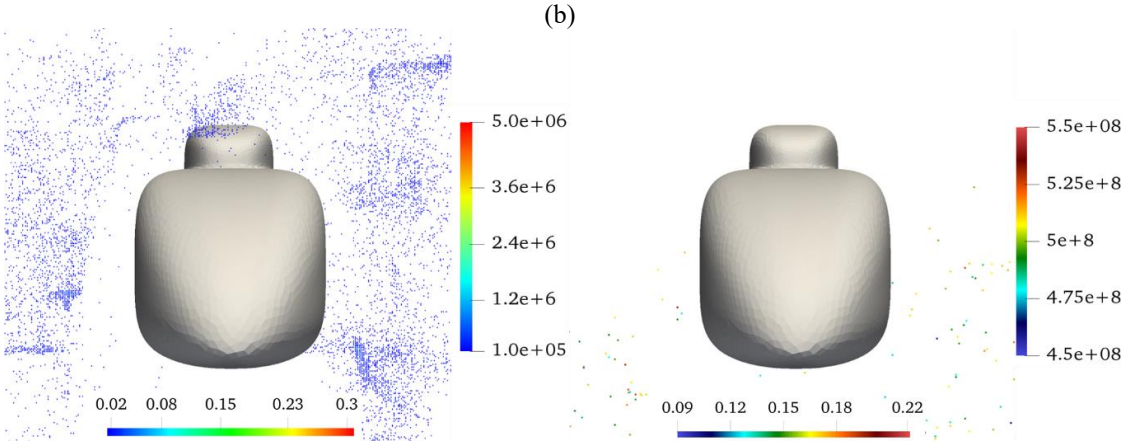

(c)

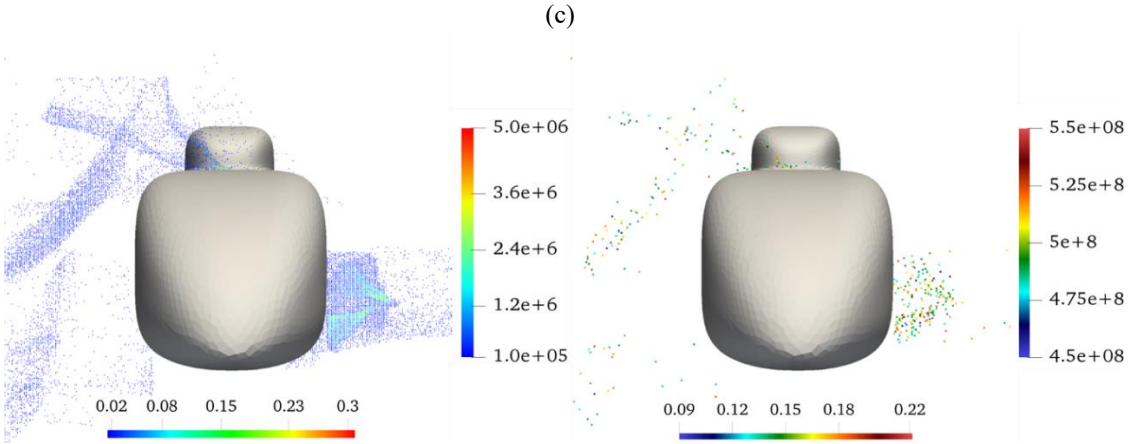

(d)

Fig. 16. Footprint and Monte Carlo probability density for different ice shapes: (a) plate, (b) disc, (c) ellipse, and (d) GIS. The vertical numbers represent the actual hits, while the horizontal numbers represent the corresponding percentage.

3.4.2. Footprint analysis of the tail rotor plane

The tail rotor is another rotorcraft critical component, susceptible to external foreign object damage (FOD). We conducted trajectory analysis and Monte Carlo simulations of ice fragment to investigate the effect of the flow fields and ice shapes on the tail rotor plane. Because of its rearmost location and relatively small size, the tail rotor does not affect the overall flow field compared to the main rotor. Thus the tail rotor was ignored in the airflow simulation. The main rotor blade of the rotorcraft uses electrothermal de-icing rather than anti-icing, because it has high energy consumption efficiency. After considering the de-icing mechanism, the five break-off locations of the ice fragments were assumed to be equally distributed on the outer half of the main rotor blade. We only considered the blade approaching towards the tail rotor (every 30 degrees), resulting in seven cases in total. The direction of the moving ice fragment and the relative velocity between the ice fragment and the tail rotor are essential properties needed to measure the potential for damage due to the external FOD.

Effect of flow conditions

The overall direction of the downwash was found to be the main factor driving ice fragment movement towards the tail rotor. In Fig. 17, I, II, III, and IV describe the direction of the downwash for advance ratios of 0.2, 0.15, 0.075, and hovering, respectively. As the advance ratio increased, the wake-skew angle increased. As a result, there is very small or no interaction with the tail region of the rotorcraft, leading to lower footprint density and Monte Carlo probability density.

At a low advance ratio, more of the air flow moves with the downwash and interacts with the tail region. When hovering, the downwash moves downwards vertically and has a symmetric pattern. The main rotor vortex and the secondary vortex (the vortex generated by the interaction

between the main vortex and rotorcraft structure) interact strongly with the tail region. As a result, the density pattern is compact at the tail rotor plane, and the Monte Carlo probability density reaches maximum.

In summary, for the probability density pattern, the effect of the flow field on the tail rotor is opposite to that on the engine intake plane. High-speed flight increases the probability density on the engine intake, whereas hovering and low-speed flight increase the probability density on the tail rotor.

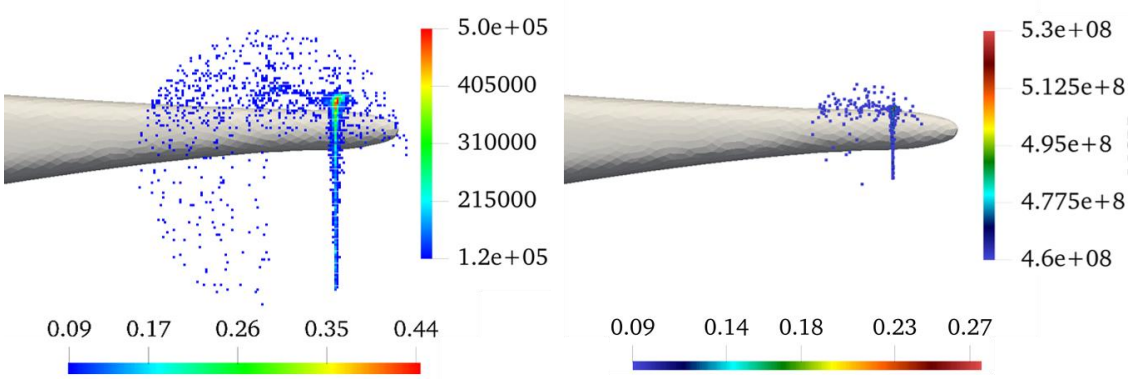

(a)

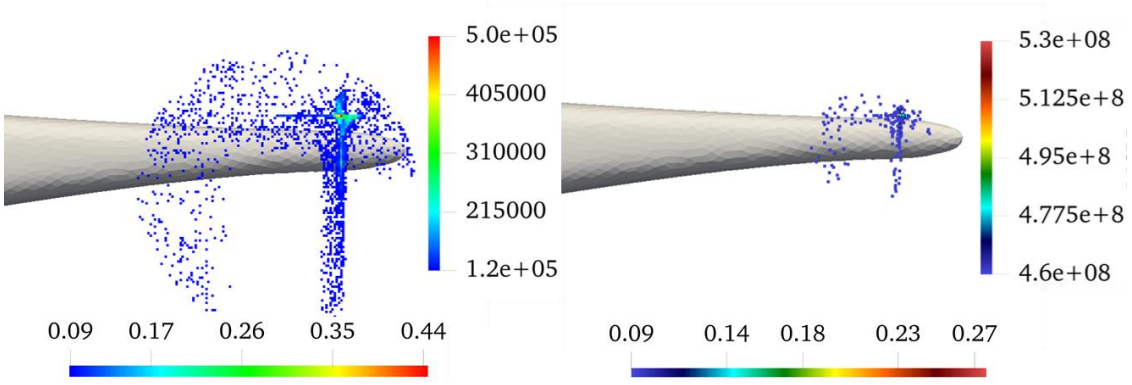

(b)

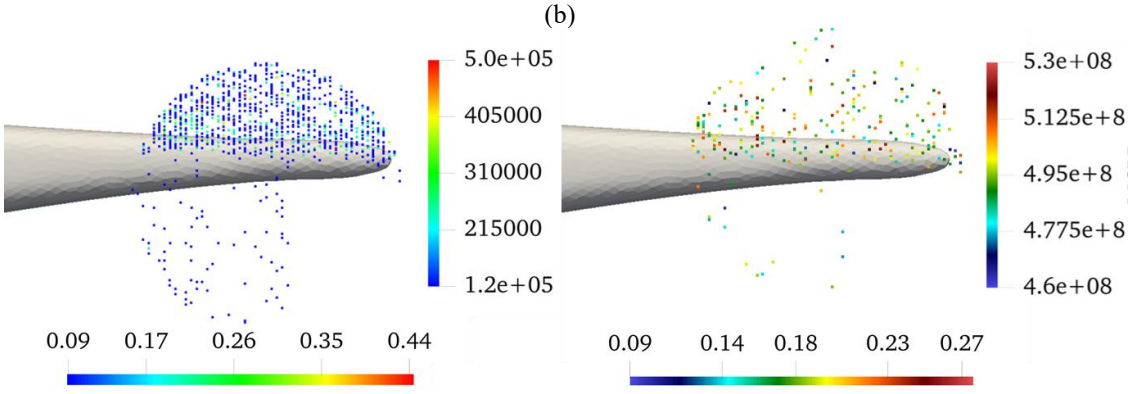

(c)

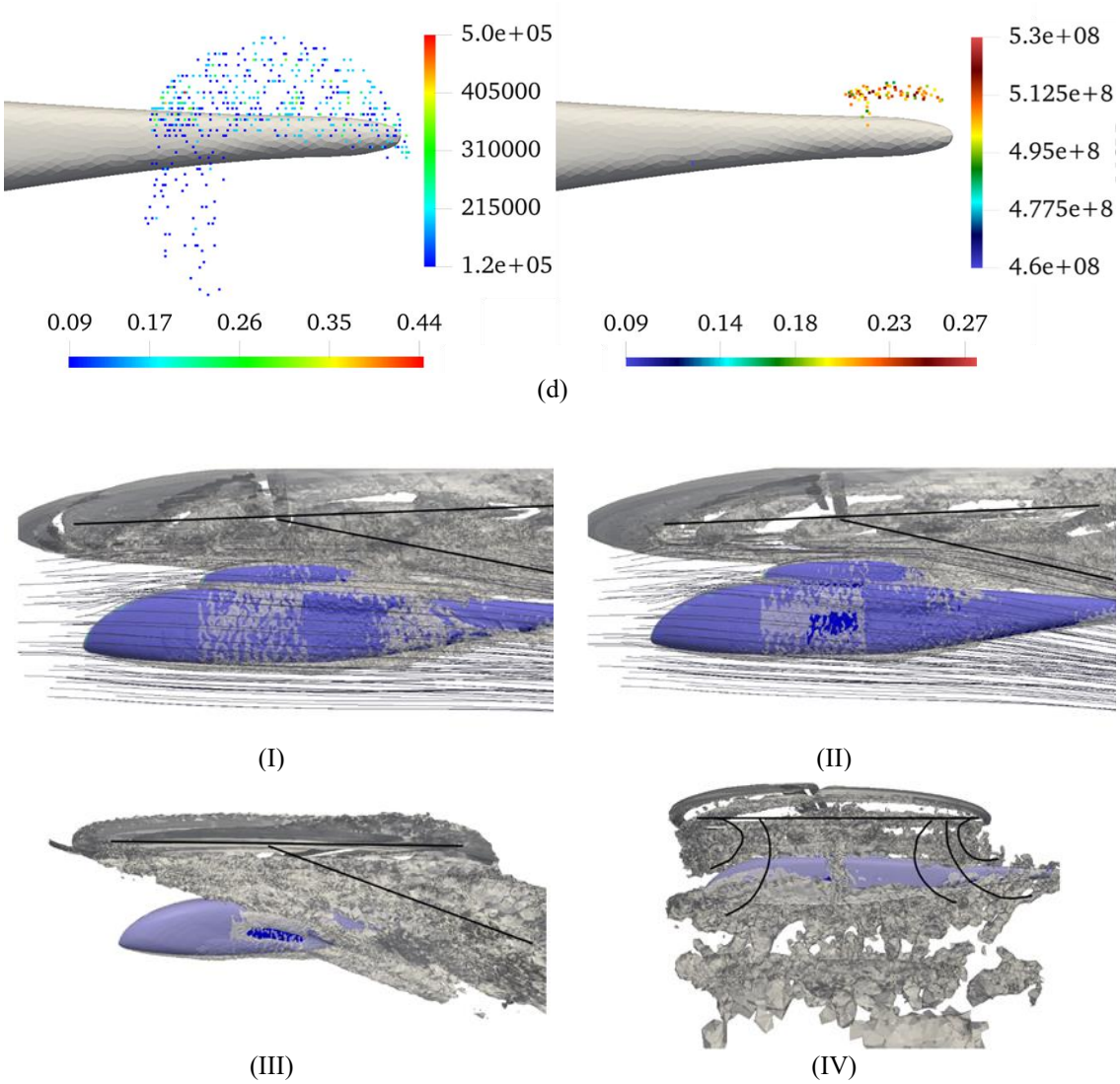

Fig. 17. Footprint density (left) and Monte Carlo probability density (right) for different advance ratios: (a) μ=0.2, (b) μ=0.15, (c) μ=0.075, and (d) μ=0.0. The vertical numbers represent the actual hits, while the horizontal numbers represent the corresponding percentage. I, II, III, and IV visualize the wakes in the corresponding flow fields.

Effect of ice shapes

The shape of the ice accreted on the rotor blade is sensitive to the rotational speed of the rotor, advance ratio, location, airfoil section, and meteorological icing conditions [77]. The ice shape is also affected by the activation of the electrothermal de-icing system, which removes the accreted ice periodically from the rotor blade. Consequently, the ice shapes shed from the rotor blade may

be very diverse—for example, thin in heat mode and thick in case of the failure of the de-icing system. Therefore, as a starting point we can apply the same representative ice shapes which were originally derived by considering the fuselage. Figure 18 shows that the general trend in density on the tail rotor plane was slightly different than that on the engine intake plane. The GIS ice showed the highest Monte Carlo probability density, followed by the plate-shaped ice, the disc-shaped ice, and lastly the elliptic shape ice.

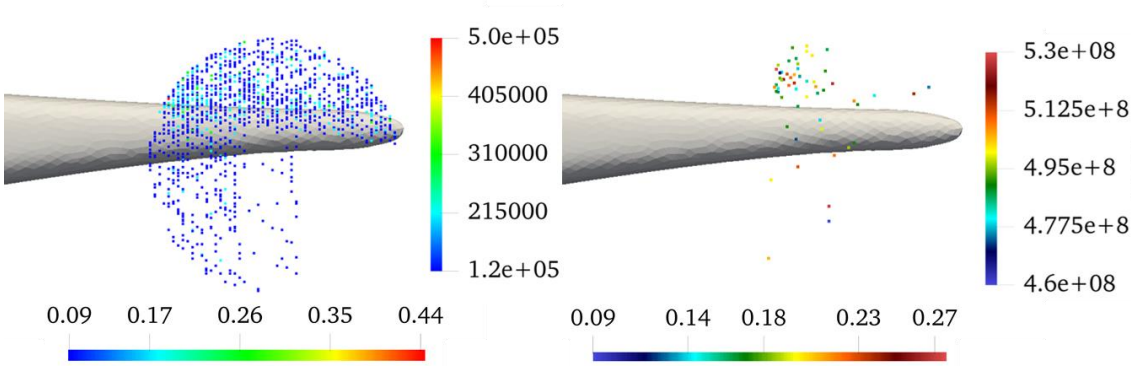

(a)

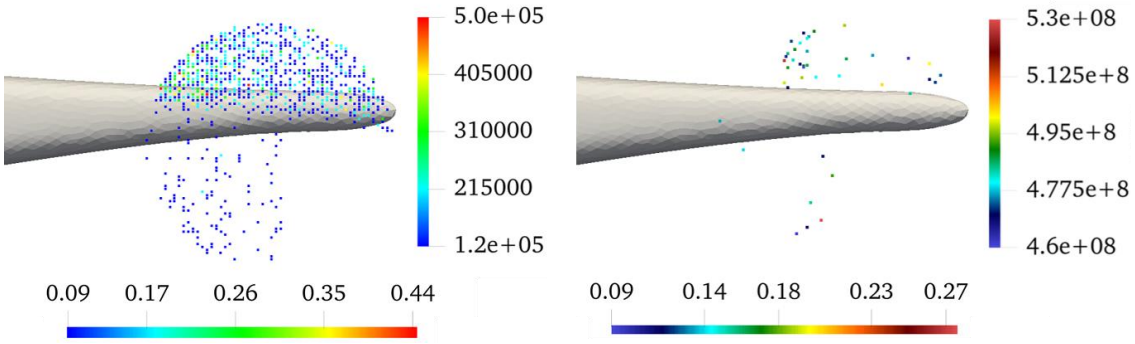

(b)

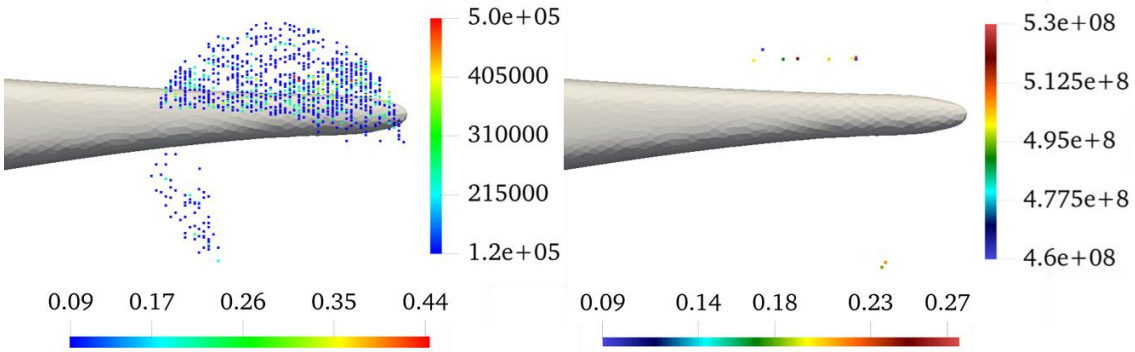

(c)

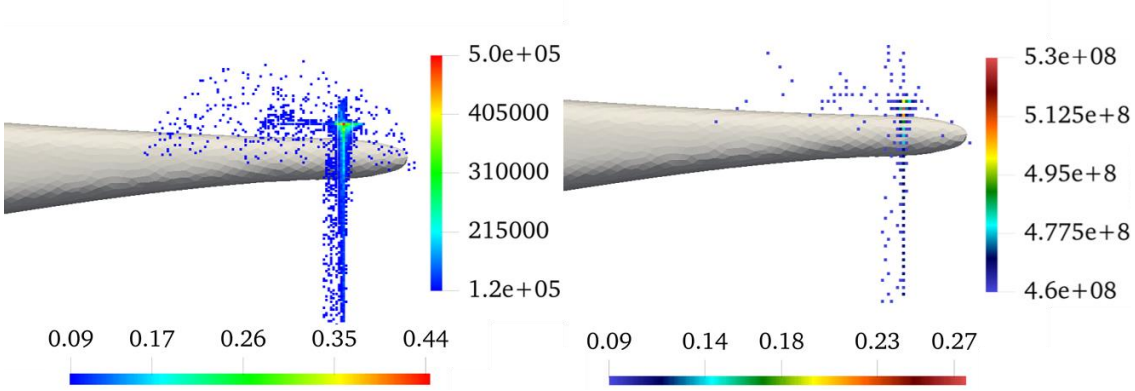

(d)

Fig. 18. Footprint density (left) and Monte Carlo probability density (right) for different ice shapes: (a) plate, (b) disc, (c) ellipse, and (d) GIS. The vertical numbers represent the actual hits, while the horizontal numbers represent the corresponding percentage.

4. Ice shedding characteristics in rotorcraft

Ice shedding can disrupt engine operation when the ice fragment is ingested into the engine intake. It can also cause an external FOD when the ice fragment hits a critical component like the tail rotor. Based on the extensive studies described in the previous sections, we shall discuss characteristics and implications of ice shedding in this section.

4.1. Hovering

Ice shedding during hovering was not critical to the engine intake of the rotorcraft. There was no trajectory footprint on the engine intake plane, because of the blocking effect of the strong downwash in the vertical direction. Computational simulations showed that very few or no fragments reached the engine intake plane. The vortex resulting from the rotation of the rotor blades directly affects the flow around the rotorcraft structure. Because of the strong unidirectional downward airflows, the ice fragments, even with a very high pitch angle, could not reach the engine intake plane. The fragments either collided with the surface long before reaching the engine intake plane, or they moved in the downward direction due to the direction of airflow and gravity.

On the other hand, the tail rotor can be vulnerable to external FOD, since several vortices of

several scales generated from the interaction of the main vortex and the tail region make it possible for ice fragments to reach the tail rotor. Nonetheless, since the ice fragment moves with relatively low velocity, ice shedding in the hovering condition may not be critical for the tail rotor of the rotorcraft.

4.2. Forward flight

Unlike fixed-wing aircraft, a rotorcraft has an asymmetric, vortex-dominated, high spatially varying flow field. As mentioned earlier, aerodynamic forces and moments acting on an ice fragment are proportional to the square of the relative velocity of the airflow and ice fragment. With increasing advance ratio, the relative velocity also increases, resulting in high aerodynamic forces and moments. Flight at high forward speed in icing conditions proved to be dangerous for sensitive components of the rotorcraft, especially the engine intake.

It was shown that the fragment resembling disc-shaped ice with a sharp edge was the most hazardous ice shape. Two other parameters—initial break-off locations and advance ratios—played non-negligible roles. The ice shed from the centerline of the fuselage (for example, the upper part of the windshield) turned out to be the most dangerous location. A significant percentage of ice fragments from this location hit the engine intake. On the other hand, because of the asymmetric flow-field caused by the rotation of the rotor, the trajectories of ice shed from opposite sides of the fuselage (B and D or C and E in Fig. 5) were found to be substantially different. Because of the counterclockwise rotor rotation, the left side of the rotorcraft (viewed from the front) encounters more adverse effects from ice shedding. This aspect may be taken into consideration when selecting the location of ice detectors on rotorcraft.

Tail rotors are designed to withstand bird strikes of up to a one-kilogram bird. According to 14 CFR § 29.631, the velocity of the rotorcraft is VNE (Never exceed speed) or VH (Maximum speed in level flight at maximum continuous power), whichever is lesser [78]. Since the energy of the impact is proportional to the square of the impact velocity, low velocity causes a low impact. Therefore, low speed flight is recommended during icing conditions, even though the probability density on the tail rotor plane at low speed is greater than that of high speed. Low speed flight

during icing conditions is safer for the engine as well as the tail rotor [79-81]. In the event of an inevitable collision between ice fragments and the tail rotor, the kinetic energy of the ice fragment should not exceed the kinetic energy of a one-kilogram bird strike.

5. Further issues in developing safety enhancement measures for rotorcraft

In this section, we discuss further issues in developing measures to enhance the safety of rotorcraft during icing conditions.

5.1. Integrated computational simulation for designing the rotorcraft IPS

The flow field of a rotorcraft in forward flight has an enormous impact on ice ingested into the engine intake and the external FOD to the tail rotor. The actuator disc method [82] is commonly used to model the rotor blade effect. Although this method is computationally very efficient, it is unable to model the effect of strong rotor wakes associated with multiple rotor blades and their impact on ice accretion on the fuselage. Wang *et al*. [83] reported a recent development in the study of ice accretion on a rotor blade in forward flight with overset grids. Son *et al*. [84] studied ice accretion on wind turbine blades by applying the multiple reference frame approach.

Available power for anti-icing and de-icing is limited in rotorcraft. For the electrothermal anti-icing systems for the engine intake and the windshield, it is essential to keep power consumption low. On the other hand, for the electrothermal de-icing systems for the main rotors, proper intervals of power on/off time are critical to minimize runback ice. Simply maintaining the power-on state longer could cause more runback ice, making the de-icing less effective. Therefore, an accurate computation of ice accretion and shedding using an integrated simulation for the fuselage and main rotor will play an essential role in the proper design of the IPS. Further, accurate information about the amount and location of ice accretion will help to quantify the power required for the IPS.

5.2. Localized evaporative heating

Anti-icing systems prevent ice forming and adhering to the surface of a structure. These systems can be run in either wet or dry conditions. In wet conditions anti-icing systems require

less energy and do not evaporate all of the water. The unevaporated water travels downstream due to aerodynamic drag and refreezes again as run-back ice and form ridges. In contrast, in dry conditions, all of the water evaporates before it reaches the cold area.

Anti-icing can be achieved in three ways, either by hot air obtained from hot air bypass from the engine or using a fluid system where freezing point depressant chemicals are used, or by an electrothermal system where energy is supplied from the generator [85].

Electrothermal heating systems [86] consist of heating pads or films. Although the generator is required for operation, their system efficiency is higher than other anti-icing systems such as hot air. The power distribution can be customized and can be used in both dry and wet conditions. At the same time, the computational simulations can be used to optimize the power distribution of the anti-icing systems.

In the present study, it was found that the ice shed from the upper edge of the windshield was most dangerous, along with the sides of the windshield. Therefore, the ice shed from these locations must be minimized, and it should not be allowed to form disc-shaped ice with a sharp edge. Fully evaporative anti-icing systems in these locations can increase the safety of the rotorcraft during icing conditions by preventing the formation of run-back ice or ridges.

5.3. Automation system based on varying and localized IPS power distribution

A sophisticated automation system can be developed to minimize energy consumption and cover the diverse forms of icing that might be encountered. Bragg *et al*. [87] proposed an icing encounter automation system based on ice accretion sensors, IPS, an interface unit, and an ice management system (IMS). Ice accretion sensors are responsible for the detection of ice on the rotorcraft. After receiving the ice accretion information, the information is transferred to the IMS and interface unit. If the pilot activates the IPS, this is known as advisory operation. But if the IMS activates IPS, it is referred to as primary IPS operation. IMS is the main unit, which is connected to sensors, an interface unit, and a feedback loop from IPS, as shown in Fig. 19.

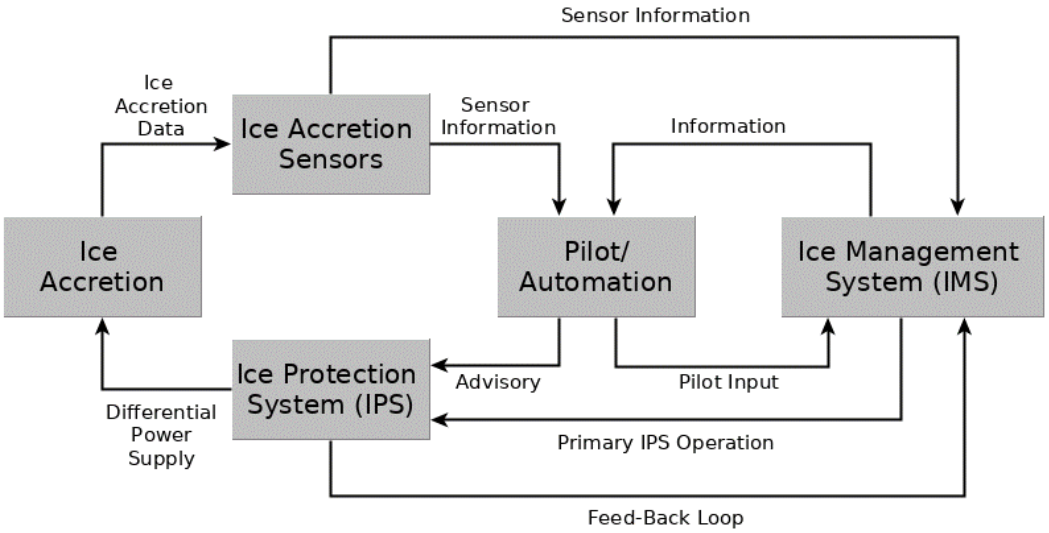

Fig.19. Rotorcraft icing encounter automation model.

The concept proposed in this study is intended to work in unison with the IPS to provide an additional level of safety beyond that provided by a simple IPS system. For a variety of reasons, rotorcraft cannot always avoid ice and as a result can encounter situations that could jeopardize the safety of the rotorcraft. Therefore, additional safety measures beyond current levels are advisable for a meaningful reduction in icing-related accidents.

The function of the IMS can be summarized as follows:

1. To sense the presence of ice accretion in various locations based on the information obtained by ice accretion sensors.

2. Automatically activate the IPS based on the amount of ice accretion detected, using a variable power supply for the electrothermal heating pads or films. Also, provide feedback to the pilot system status.

3. IMS will operate based on data from the IPS and the ice accretion sensor. Based on the severity of ice detected by the sensors, the power supply to the IPS will be controlled.

It is known that ice accretion on the engine intake and the windshield of the fuselage differs with location. If the heating mats (embedded in the engine intake) or the heating thin film (embedded in the windshield) are provided with the same power for all protected regions, it may cause an inefficient usage of power due to variations in ice accretion, as shown in Fig. 8. To address

this problem, integrated computational simulation can be used to identify the areas more sensitive to ice accretion. For example, the present study showed that the upper part of the windshield is a sensitive location for ice shedding. These areas can be appropriately identified at the design stage and locally provided with varying amounts of power, sufficient to prevent the build-up of dangerous ice shapes like the disc-shaped with sharp edges. This will substantially enhance the energy efficiency of the IPS and can prevent ice shedding from the outset.

5.4. Windshield wiper design

An ingrained problem that exists in the operation of helicopters during winter is the build-up of ice on the windshield and wipers [88,89] which eventually hinders the visibility of the pilot. Although heaters are provided within layers, there may be insufficient transfer of heat through the glass of the windshield from inside, causing the ice to build-up. After a sufficient accumulation of ice on the windshield, visibility can be severely impaired.

Over the years, several methods have been proposed to improve the operation of the windshield wiper in icing conditions. The windshield wiper system is sometimes provided with a slapping activated mechanism [90] that allows the wiper blades to slap against the windshield causing the built-up ice (and snow) to fall away. This mechanism is pilot-driven in case of need. Although this kind of system is successful at removing ice from windshield and wiper, there is a great possibility that the broken built-up ice fragments will be carried by the downstream airflow and hit critical components of the rotorcraft.

Another common practice in the design of windshield wipers for cold climates is to provide a chemical washing fluid that removes the ice [91]. Wipers are equipped with primary nozzles to provide washing fluid during normal operation and secondary nozzles to bathe the wiper during de-icing. In this kind of system, a control unit is needed to automatically operate the wiper motor, fluid pump, and for temperature detection. To modify this kind of system, various chemical fluids can be used for ice washing.

There are a couple of patents on a windshield wiper with a heater assembly made up of electrical heating elements along the longitudinal length [92,93]. An electric current is passed

through the coils of the heating element producing heat along the length of the wiper. The heat helps the ice to melt on the wiper and as well on the windshield. If more heat is provided on the outer radius of the wiper, it can minimize the shedding of ice towards the engine intake. In this case, an integrated computational simulation can be used to optimize the power distribution of the windshield wiper, and a windshield embedded with electrothermal thin films. Moreover, such a windshield wiper system can be integrated with the IMS, which can effectively melt the ice on the windshield and modulate the power, based on requirements.

6. Conclusions and remarks

Ice shedding from rotorcraft is a safety concern since it can cause considerable damage to the engine and other sensitive rotorcraft components. We developed a general methodology to predict the location of ice accretion and break-off, ice shape and shedding trajectory in the rotorcraft flow field with strong rotor wakes in forward flight. The ice accretion simulation method consists of four modules: 1) a flow analysis module based on the NSF equations and the actuator surface method, 2) a droplet-trajectory analysis module based on the Eulerian droplet equation, 3) a PDE-based thermodynamic module, and 4) a grid-regeneration module. Other modules include the aerodynamic database for different ice shapes at various combinations of Euler angles, and a six degree-of-freedom trajectory analysis using artificial neural networks and the Monte Carlo method.

High speed forward flight in icing conditions proved to be the most dangerous for sensitive components of rotorcraft, especially the engine intake. In particular, it is necessary to minimize the runback ice shed from the upper edge of the windshield and the lip of the engine intake by installing proper IPS in those regions. For this task, integrated computational simulation can be used to optimize the power distribution of the windshield and the engine intake equipped with electrothermal anti-icing systems.

Disc-shaped ice fragments with a sharp edge turned out to be most dangerous. The rotation of the main rotors also substantially affected ice accretion and shed trajectory, indicating the importance of conducting integrated simulations of all components of the rotorcraft when designing rotorcraft ice protection systems. When inevitable collisions occurred between ice

fragments and the tail rotor, the situation was not serious in most cases, since the kinetic energy of the ice fragment impact was much lower than the kinetic energy associated with a bird strike.

In this study, among various types of rotorcraft engine intake, we considered the conventional Pitot-type intake, which is located at the front of the upper fuselage and can thus take full advantage of high dynamic pressure in forward flight. If a side-mounted intake is considered, there will be a substantial change in the ice accretion and shedding characteristics. In addition, it will be very interesting to investigate the ice accretion and shedding problems on new platforms such as compound helicopters and urban air mobility vehicles. We hope to report the results of our study of these problems in the future.

Acknowledgments

This work was supported by the National Research Foundation of Korea (NRF) Grant funded by the Ministry of Science, ICT & Future Planning (NRF-2017-R1A5A1015311), South Korea.

Appendix A. Eulerian description of the droplet flow field

The present droplet-trajectory module is based on the Eulerian approach. Aerodynamic drag, buoyancy, and gravity acting on the droplet field can be treated as source terms in the following equations of mass and momentum conservation,

$$\begin{bmatrix} \rho_d \\ \rho_d \vec{u}_d \end{bmatrix}_t + \nabla \cdot \begin{bmatrix} \rho_d \vec{u}_d \\ \rho_d \vec{u}_d \vec{u}_d \end{bmatrix} = \begin{bmatrix} 0 \\ \dfrac{3}{4} \dfrac{\rho_d \mu_a C_D \,\mathrm{Re}_d}{\rho_w MVD^2} \left(\vec{u}_a - \vec{u}_d \right) + \rho_d \vec{g} \left(1 - \dfrac{\rho_a}{\rho_w} \right) \end{bmatrix}. \tag{A1}$$

Here the subscripts *d*, *a*, *w* denote droplet, air, and water, respectively. The Reynolds number of a droplet is defined as $\mathrm{Re}_d = \rho_a \cdot MVD \cdot \left| \vec{u}_a - \vec{u}_d \right| / \mu_a$. In atmospheric icing conditions, the ratio of the mass of water droplets of small size (approximately a few tens of micrometers in diameter) to the mass of air in unit volume is known to be in the range of 10^{-3}. In addition, the corresponding Stokes number—characterizing the behavior of particles suspended in a fluid flow—inside a cloud

composed of air and small super-cooled droplets of liquid water is known to be smaller than 0.1 in most flight conditions. Therefore, the air-mixed droplet multiphase flow field can be solved using a weakly coupled (one-way coupling) algorithm, meaning that the droplet field may be calculated separately from the air flow field. Once the droplet flow field is known, the mass rate of droplets impinging on the surface can be determined as follows,

$$\dot{m} = \rho_d \vec{u}_d \cdot \vec{n} \tag{A2}$$

where $\vec{n}$ is the local surface normal vector.

Appendix B. Thermodynamic ice accretion solver

The mass of an impinging droplet can be computed from the velocity and bulk density of the droplet field. The role of the thermodynamic analysis module is to determine the fraction of the mass that freezes on the surface. To explain the behavior of unfrozen water on the surface in case of glaze ice, a theory of thin water film is necessary. Since the water film is thin in ice simulations, the velocity profile of the water film is linear. Consequently, the velocity of the thin water film can be written as a function of the wall shear stress and water film thickness,

$$\bar{U}_f = \frac{1}{h_f}\int_0^{h_f} u_f dh = \frac{h_f}{2\mu_w}\vec{\tau}_{wall}\,. \tag{B1}$$

The convection terms in the mass- and energy-conservation equations are related to the fraction of water that does not freeze. The net flux of the water film in the control volume can be calculated in the same manner as the flow solver,

$$\begin{bmatrix} h_f \\ h_f C_{p,w}\tilde{T}_{eq} \end{bmatrix}_t + \nabla \cdot \begin{bmatrix} h_f \bar{U}_f \\ h_f C_{p,w}\tilde{T}_{eq}\bar{U}_f \end{bmatrix} = \frac{1}{\rho_w}\begin{bmatrix} \dot{m} - \dot{m}_{ice} \\ \dot{m}\left(C_{p,w}\tilde{T}_{eq} + \frac{1}{2}U_d{}^2\right) \\ -\dot{m}_{ice}\left(L_{fus} - C_{p,i}\tilde{T}_{eq}\right) + h_c\left(T_{eq} - T_\infty\right) \end{bmatrix}. \tag{B2}$$

The first-term on the right side of the first equation represents the water mass that hits the surface,

while the second-term shows the ice mass that freezes on the surface. The first-term on the right-hand side of the second equation represents the kinetic energy of the water droplet, while the second- and third-terms represent the latent heat and heat convection, respectively.

The clean air solver provides the wall shear stress and heat transfer coefficient (h_c) as inputs to the ice accretion solver. The shallow water type (A1) droplet solver provides the droplet impact velocity and collection efficiency as inputs to the ice accretion solver. There are three unknowns to be computed: water film thickness h_f, equilibrium temperature $\tilde{T}_{eq}$, and mass accumulation $\dot{m}_{ice}$. Since there are only two governing equations available in (B2), compatibility relations are necessary to close the system. Based on physical behavior, the following compatibility equations proposed by Beaugendre *et al*. [27] can be used:

$$\begin{cases} h_f \geq 0 \\ \dot{m}_{ice} \geq 0 \\ h_f \tilde{T}_{eq} \geq 0 \\ \dot{m}_{ice} \tilde{T}_{eq} \geq 0 \end{cases} \tag{B3}$$

Finally, the ice thickness is determined by dividing the calculated mass of ice by the ice density in the grid-regeneration module.

References

[1] *Technically Advanced Aircraft-Safety and Training*, Special Report, AOPA Air Safety Foundation, USA, 2005.

[2] S. M. Jones, M. S. Reveley, J. K. Evans, and F. A. Barrientos, "Subsonic aircraft safety icing study," *NASA/TM—2008–215107*, 2008.

[3] D. Ignatyev, A. N. Khrabrov, A. Kortukova, D. Alieva, M. E. Sidoryuk, and S. G. Bazhenov, "Interplay of unsteady aerodynamics and flight dynamics of transport aircraft in icing conditions," *Aerospace Science and Technology,* 105914, 2020.

[4] G.-q. Zhao, Q.-j. Zhao, and X. Chen, "New 3-D ice accretion method of hovering rotor including effects of centrifugal force," *Aerospace Science and Technology,* vol. 48, pp. 122-130, 2016.

[5] Y. Cao, W. Tan, and Z. Wu, "Aircraft icing: an ongoing threat to aviation safety,"

Aerospace Science and Technology, vol. 75, pp. 353-385, 2018.

[6] T. P. Ratvasky, B. P. Barnhart, and S. Lee, "Current methods modeling and simulating icing effects on aircraft performance, stability, control," *Journal of Aircraft,* vol. 47, no. 1, pp. 201-211, 2010.

[7] K. D. Korkan, L. Dadone, and R. J. Shaw, "Performance degradation of helicopter rotor in forward flight due toice," *Journal of Aircraft,* vol. 22, no. 8, pp. 713-718, 1985.

[8] K. Korkan, E. Cross Jr, and T. Miller, "Performance degradation of a model helicopter rotor with a generic ice shape," *Journal of Aircraft,* vol. 21, no. 10, pp. 823-830, 1984.

[9] M. Papadakis, H.-W. Yeong, and I. Suares, "Simulation of ice shedding from a business jet aircraft," in *45th AIAA Aerospace Sciences Meeting and Exhibit*, 2007.

[10] M. Potapczuk, K. Al-Khalil, and M. Velazquez, "Ice accretion and performance degradation calculations with LEWICE/NS," in *31st Aerospace Sciences Meeting*, 1993.

[11] W. Wright, "Validation results for LEWICE 3.0," in *43rd AIAA Aerospace Sciences Meeting and Exhibit*, 2005.

[12] T. Hedde and D. Guffond, "ONERA three-dimensional icing model," *AIAA Journal,* vol. 33, no. 6, pp. 1038-1045, 1995.

[13] K. Nakakita, S. Nadarajah, and W. Habashi, "Toward real-time aero-icing simulation of complete aircraft via FENSAP-ICE," *Journal of Aircraft,* vol. 47, no. 1, pp. 96-109, 2010.

[14] Y. Bourgault, Z. Boutanios, and W. G. Habashi, "Three-dimensional Eulerian approach to droplet impingement simulation using FENSAP-ICE, Part 1: model, algorithm, and validation," *Journal of Aircraft,* vol. 37, no. 1, pp. 95-103, 2000.

[15] E. Lozowski, J. Stallabrass, and P. Hearty, "The icing of an unheated, nonrotating cylinder. Part Ii. Icing wind tunnel experiments," *Journal of Climate and Applied Meteorology,* vol. 22, no. 12, pp. 2063-2074, 1983.

[16] G. Fortin and J. Perron, "Spinning rotor blade tests in icing wind tunnel," in *1st AIAA Atmospheric and Space Environments Conference*, 2009.

[17] C. Mayer, A. Ilinca, G. Fortin, and J. Perron, "Wind tunnel study of electro-thermal de-icing of wind turbine blades," *International Journal of Offshore and Polar Engineering,* vol. 17, no. 03, 2007.

[18] M. Papadakis, H.-W. Yeong, S.-C. Wong, M. Vargas, and M. Potapczuk, *Experimental Investigation of Ice Accretion Effects on a Swept Wing*, DOT/FAA/AR-05/39, Federal Aviation Administration, 2005.

[19] M. Papadakis *et al.*, *Experimental Investigation of Water Droplet Impingement on Airfoils, Finite Wings, and an S-duct Engine Inlet*, National Aeronautics and Space Administration, Glenn Research Center, 2002.

[20] T. P. Ratvasky, J. F. Van Zante, and A. Sim, "NASA/FAA tailplane icing program: Flight test report," *NASA-TP-2000-209908*, 2000.

[21] R. Shaw and G. Richter, "The UH-1H helicopter icing flight test program-An overview," in *23rd Aerospace Sciences Meeting*, 1985.

[22] G. Isaac, S. Cober, J. Strapp, A. Korolev, A. Tremblay, and D. Marcotte, "Recent Canadian research on aircraft in-flight icing," *Canadian Aeronautics and Space Journal,* vol. 47, no. 3, pp. 213-221, 2001.

[23] M. Papadakis, H.-W. Yeong, K. Shimoi, and S.-H. Wong, "Ice shedding experiments with simulated ice shapes," in *1st AIAA Atmospheric and Space Environments Conference*, 2009.

[24] D. Kohlman and R. Winn, "Analytical prediction of trajectories of ice pieces after release in an airstream," in *39th Aerospace Sciences Meeting and Exhibit*, 2001.

[25] S. Murman, M. Aftosmis, and M. Berger, "Simulations of 6-DOF motion with a Cartesian method," in *41st Aerospace Sciences Meeting and Exhibit*, 2003.

[26] W. B. Wright, R. Gent, and D. Guffond, "DRA/NASA/ONERA collaboration on icing research. Part 2; prediction of airfoil ice accretion," *NASA-CR-202349*, 1997.

[27] H. Beaugendre, F. Morency, and W. G. Habashi, "FENSAP-ICE's three-dimensional in-flight ice accretion module: ICE3D," *Journal of Aircraft,* vol. 40, no. 2, pp. 239-247, 2003.

[28] L. P. Raj, J. Lee, and R. S. Myong, "Ice accretion and aerodynamic effects on a multi-element airfoil under SLD icing conditions," *Aerospace Science and Technology,* vol. 85, pp. 320-333, 2019.

[29] L. P. Raj, K. Yee, and R. S. Myong, "Sensitivity of ice accretion and aerodynamic performance degradation to critical physical and modeling parameters affecting airfoil icing," *Aerospace Science and Technology,* vol. 98, 105659, 2020.

[30] S. Jung, L. P. Raj, A. Rahimi, H. Jeong, and R. S. Myong, "Performance evaluation of electrothermal anti-icing systems for a rotorcraft engine air intake using a meta model," *Aerospace Science and Technology*, vol. 106, 106174, 2020.

[31] Y. Cao and K. Chen, "Helicopter icing," *The Aeronautical Journal,* vol. 114, no. 1152, pp. 83-90, 2010.

[32] K. Szilder, "Numerical simulation of ice formation on a helicopter fuselage," *SAE Technical Paper 0148-7191*, 2007.

[33] C. N. Aliaga, M. S. Aubé, G. S. Baruzzi, and W. G. Habashi, "FENSAP-ICE-Unsteady: unified in-flight icing simulation methodology for aircraft, rotorcraft, and jet engines," *Journal of Aircraft,* vol. 48, no. 1, pp. 119-126, 2011.

[34] G. Ahn, K. Jung, R. S. Myong, H. Shin, and W. Habashi, "Numerical and experimental investigation of ice accretion on rotorcraft engine air intake," *Journal of Aircraft,* vol. 52, no. 3, pp. 903-909, 2015.

[35] Y. M. Lee, J. H. Lee, L. P. Raj, J. H. Jo, and R. S. Myong, "Large-eddy simulations of complex aerodynamic flows over multi-element iced airfoils," *Aerospace Science and*

Technology, vol. 109, 106417, 2021.

[36] S. Nix, S. Buckner, and R. Cercone, "A review of risk analysis and helicopter air ambulance accidents," *Air Medical Journal,* vol. 33, no. 5, pp. 218-221, 2014.

[37] *Aviation Investigation Report A12P0008*, The Transportation Safety Board of Canada, British Columbia, 2012. Accessed on 11 March 2021; https://www.tsb.gc.ca/eng/rapports-reports/aviation/2012/a12p0008/a12p0008.pdf

[38] K. Ignatowicz, F. Morency, and P. Lopez, "Dynamic moment model for numerical simulation of a 6-DOF plate trajectory around an aircraft," *Journal of Aerospace Engineering,* vol. 32, no. 5, p. 04019069, 2019.

[39] M. J. Anthony, M. Nathoo, Z. Zhan, W. G. Habashi, and M. Fossati, "Rotor Ice Shedding and Trajectory Analyses in Forward Flight," in *2018 Atmospheric and Space Environments Conference*, 2018.

[40] R. Hayashi and M. Yamamoto, "Numerical simulation on ice shedding phenomena in turbomachinery," in *ASME Turbo Expo 2014: Turbine Technical Conference and Exposition*, 2014.

[41] Y. Dong and J. Ai, "Research on inflight parameter identification and icing location detection of the aircraft," *Aerospace Science and Technology,* vol. 29, no. 1, pp. 305-312, 2013.

[42] N. D. Sathyanarayana and K. Hoffmann, "Trajectory prediction using coupled CFD-RBD with dynamic meshing," in *AIAA Scitech 2019 Forum*, 2019.

[43] M. Biava, W. Khier, and L. Vigevano, "CFD prediction of air flow past a full helicopter configuration," *Aerospace Science and Technology,* vol. 19, no. 1, pp. 3-18, 2012.

[44] V. Raghav and N. Komerath, "Advance ratio effects on the flow structure and unsteadiness of the dynamic-stall vortex of a rotating blade in steady forward flight," *Physics of Fluids,* vol. 27, no. 2, p. 027101, 2015.

[45] P. F. Lorber and T. A. Egolf, "An Unsteady Helicopter Rotor-Fuselage Aerodynamic Interaction Analysis," *Journal of the American Helicopter Society,* vol. 35, no. 3, pp. 32-42, 1990.

[46] F. De Gregorio, "Flow field characterization and interactional aerodynamics analysis of a complete helicopter," *Aerospace Science and Technology,* vol. 19, no. 1, pp. 19-36, 2012.

[47] F. Köpp, "Wake-vortex characteristics of military-type aircraft measured at airport Oberpfaffenhofen using the DLR laser doppler anemometer," *Aerospace Science and Technology,* vol. 3, no. 4, pp. 191-199, 1999.

[48] G. Srinivasan, V. Raghavan, E. Duque, and W. McCroskey, "Flowfield analysis of modern helicopter rotors in hover by Navier-Stokes method," *Journal of the American Helicopter Society,* vol. 38, no. 3, pp. 3-13, 1993.

[49] C. A. Ozen and D. Rockwell, "Three-dimensional vortex structure on a rotating wing,"

Journal of Fluid Mechanics, vol. 707, pp. 541-550, 2012.

[50] F. X. Caradonna and C. Tung, "Experimental and analytical studies of a model helicopter rotor in hover," *NASA-TM-81232*, 1981.

[51] M. Bross, C. Ozen, and D. Rockwell, "Flow structure on a rotating wing: effect of steady incident flow," *Physics of Fluids,* vol. 25, no. 8, p. 081901, 2013.

[52] C. Son, S. Oh, and K. Yee, "Ice accretion on helicopter fuselage considering rotor-wake effects," *Journal of Aircraft,* vol. 54, no. 2, pp. 500-518, 2017.

[53] S. K. Jung and R. S. Myong, "A second-order positivity-preserving finite volume upwind scheme for air-mixed droplet flow in atmospheric icing," *Computers & Fluids*, vol. 86, pp. 459-469, 2013.

[54] S. K. Jung and R. S. Myong, "A relaxation model for numerical approximations of the multidimensional pressureless gas dynamics system," *Computers and Mathematics with Applications*, vol. 80, no. 5, pp. 1073-1083, 2020.

[55] T. Kim, S. Oh, and K. Yee, "Improved actuator surface method for wind turbine application," *Renewable Energy,* vol. 76, pp. 16-26, 2015.

[56] Y. Chen, W. Dong, Z. Wang, and L. Fu, "Numerical simulation of ice shedding from a fan blade," in *Turbo Expo: Power for Land, Sea, and Air*, 2015.

[57] M. Schulz and M. Sinapius, "Evaluation of different ice adhesion tests for mechanical deicing systems," *SAE Technical Paper 0148-7191*, 2015.

[58] A. Work and Y. Lian, "A critical review of the measurement of ice adhesion to solid substrates," *Progress in Aerospace Sciences,* vol. 98, pp. 1-26, 2018.

[59] S. A. Snyder, E. M. Schulson, and C. E. Renshaw, "Effects of prestrain on the ductile-to-brittle transition of ice," *Acta Materialia,* vol. 108, pp. 110-127, 2016.

[60] E. M. Schulson, "The structure and mechanical behavior of ice," *JOM,* vol. 51, no. 2, pp. 21-27, 1999.

[61] M. M. Riahi, D. Marceau, C. Laforte, and J. Perron, "The experimental/numerical study to predict mechanical behaviour at the ice/aluminium interface," *Cold Regions Science and Technology,* vol. 65, no. 2, pp. 191-202, 2011.

[62] J. Petrovic, "Review mechanical properties of ice and snow," *Journal of Materials Science,* vol. 38, no. 1, pp. 1-6, 2003.

[63] Y. Chen, L. Fu, and W. Dong, "Novel Cohesive/Adhesive Ice Shedding Model for Spinner Cone," *Journal of Propulsion and Power,* vol. 34, no. 3, pp. 647-659, 2018.

[64] H. Sommerwerk and P. Horst, "Analysis of the mechanical behavior of thin ice layers on structures including radial cracking and de-icing," *Engineering Fracture Mechanics,* vol. 182, pp. 400-424, 2017.

[65] E. Bernard and R. L. Duff, *Dynamics of Flight Stability and Control*, Wiley & Sons, 1996.

[66] R. C. Nelson, *Flight Stability and Automatic Control*, WCB/McGraw Hill, New York,

1998.

[67] A. K. Jain, J. Mao, and K. M. Mohiuddin, "Artificial neural networks: A tutorial," *Computer,* vol. 29, no. 3, pp. 31-44, 1996.

[68] J. M. Zurada, *Introduction to Artificial Neural Systems*, West St. Paul, 1992.

[69] M. H. Kalos and P. A. Whitlock, *Monte Carlo Methods*, John Wiley & Sons, 2009.

[70] K. Binder, D. Heermann, L. Roelofs, A. J. Mallinckrodt, and S. McKay, "Monte Carlo simulation in statistical physics," *Computers in Physics,* vol. 7, no. 2, pp. 156-157, 1993.

[71] J. W. Elliott, S. L. Althoff, and R. H. Sailey, *Inflow Measurements Made with a Laser Velocimeter on a Helicopter Model in Forward Flight. Volume 1: Rectangular Planform Blades at an Advance Ratio of 0.15*, National Aeronautics and Space Administration, 1988.

[72] J. W. Elliott, S. L. Althoff, and R. H. Sailey, *Inflow Measurement Made with a Laser Velocimeter on a Helicopter Model in Forward Flight. Volume 2: Rectangular Planform Blades at an Advance Ratio of 0.23*, National Aeronautics and Space Administration, 1988.

[73] T. A. Dickey, *An Analysis of the Effects of Certain Variables in Determining the Form of an Ice Accretion*, AEL (Aeronautical Engineering Laboratory) 1206, Aeronautical Engineering Lab., Naval Air Experimental Station, Philadelphia, 1952.

[74] G. S. Baruzzi, P. Lagacé, M. S. Aubé, and W. G. Habashi, "Development of a shed-ice trajectory simulation in FENSAP-ICE," *SAE Technical Paper 0148-7191*, 2007.

[75] K. F. Jones, "The density of natural ice accretions related to nondimensional icing parameters," *Quarterly Journal of the Royal Meteorological Society,* vol. 116, no. 492, pp. 477-496, 1990.

[76] W. Macklin, "The density and structure of ice formed by accretion," *Quarterly Journal of the Royal Meteorological Society,* vol. 88, no. 375, pp. 30-50, 1962.

[77] C. Xi and Z. Qi-Jun, "Numerical simulations for ice accretion on rotors using new three-dimensional icing model," *Journal of Aircraft,* vol. 54, no. 4, pp. 1428-1442, 2017.

[78] F. A. R. Part, *29-Airworthiness Standards: Transport Category Rotorcraft*, Federal Aviation Administration*,* 1965.

[79] *Rotorcraft Bird Strike Working Group Recommendations to the Aviation Rulemaking Advisory Committee (ARAC)*, Federal Aviation Administration (FAA), 2017.

[80] V. K. Rayavarapu, "On the bird impact damage assessment of rotorcraft horizontal stabilizer," *Applied Composite Materials,* vol. 26, no. 1, pp. 1-13, 2019.

[81] D. C. Naik and R. V. Kumar, "Helicopter main rotor blade root end under high velocity bird impact," *Materials Today: Proceedings,* vol. 5, no. 2, pp. 4653-4668, 2018.

[82] H. Fouladi, W. G. Habashi, and I. A. Ozcer, "Quasi-steady modeling of ice accretion on a helicopter fuselage in forward flight," *Journal of Aircraft,* vol. 50, no. 4, pp. 1169-1178, 2013.

[83] Z. Wang, N. Zhao, and C. Zhu, "Numerical simulation for three-dimensional rotor icing

in forward flight," *Advances in Mechanical Engineering,* vol. 10, no. 4, 1687814018772404, 2018.

[84] C. Son, H. Koss, and T. Kim, "Development of three-dimensional icing simulation code for wind turbines," in *International Workshops on Atmospheric Icing of Structures 2019*, 2019.

[85] S. K. Thomas, R. P. Cassoni, and C. D. MacArthur, "Aircraft anti-icing and de-icing techniques and modeling," *Journal of Aircraft,* vol. 33, no. 5, pp. 841-854, 1996.

[86] A. D. Yaslik, K. J. DeWitt, and T. G. Keith, "Further developments in three-dimensional numerical simulation of electrothermal de-icing systems," *AIAA-92-0528*, 1992.

[87] M. Bragg, W. Perkins, N. Sarter, P. Voulgaris, H. Gurbacki, J. Melody, and S. McCray, "An interdisciplinary approach to inflight aircraft icing safety," in *36th AIAA Aerospace Sciences Meeting and Exhibit*, 1998.

[88] P. Render and L. Jenkinson, "Investigation into ice detection parameters for turboprop aircraft," *Journal of Aircraft,* vol. 33, no. 1, pp. 125-130, 1996.

[89] J. McCrumm, "Electrical anti-icing or aircraft windshields," *Transactions of the American Institute of Electrical Engineers,* vol. 65, no. 12, pp. 786-791, 1946.

[90] W. Wagner, *Windshield Wiper Blade Slapper Apparatus*, U.S. Patent Application No 10/740,495, 2004.

[91] C. Fonville and M. Karram, *Windshield Wiper De-icing*, U.S. Patent Application No 10/867,584, 2005.

[92] R. R. Guell, *Electrically Heated Wiper Blade Utilizing Spiral Coiled Resister Wire*, U.S. Patent No 5,504,965, 1996.

[93] R. W. Malone, *Frameless, Heated Wiper Assembly and System Utilizing Same*, U.S. Patent No 7,721,382, 2010.